

A finite volume shock-capturing solver of the fully coupled shallow water-sediment equations

Maggie J. Creed^{1*}, Ilektra-Georgia Apostolidou², Paul H. Taylor², and Alistair G.L. Borthwick¹

¹ School of Engineering, The University of Edinburgh, The King's Buildings, Edinburgh EH9 3JL, U.K.

² Department of Engineering Science, University of Oxford, Parks Road, Oxford OX1 3PJ, U.K.

SUMMARY

This paper describes a numerical solver of well-balanced, 2D depth-averaged shallow water-sediment equations. The equations permit variable horizontal fluid density and are designed to model water-sediment flow over a mobile bed. A Godunov-type, HLLC finite volume scheme is used to solve the fully coupled system of hyperbolic conservation laws which describe flow hydrodynamics, suspended sediment transport, bedload transport and bed morphological change. Dependent variables are specially selected to handle the presence of the variable density property in the mathematical formulation. The model is verified against analytical and semi-analytical solutions for bedload transport and suspended sediment transport, respectively. The well-balanced property of the equations is verified for a variable-density dam break flow over discontinuous bathymetry. Simulations of an idealised dam-break flow over an erodible bed are in excellent agreement with previously published results ([1]), validating the ability of the model to capture the complex interaction between rapidly varying flow and an erodible bed and validating the eigenstructure of the system of variable-density governing equations. Flow hydrodynamics and final bed topography of a laboratory-based 2D partial dam breach over a mobile bed are satisfactorily reproduced by the numerical model. Comparison of the final bed topographies, computed for two distinct sediment transport methods, highlights the sensitivity of shallow water-sediment models to the choice of closure relationships. Copyright © 0000 John Wiley & Sons, Ltd.

Received ...

KEY WORDS: Shallow water-sediment equations, Riemann solver, finite-volume, fully-coupled, suspended sediment, bedload

1. INTRODUCTION

Accurate prediction of sediment-carrying shallow water flows is of great importance in river basin management; the context includes flood risk owing to breaching and overtopping of flood defences, bank erosion, water quality, transport of contaminants and long-term geomorphic changes to the river basin. Presence of sediment can have a significant effect on the flow hydraulics, particularly when in suspension at high concentrations (e.g. [1, 2, 3]). Urban floods and debris flows often carry substantial quantities of sediment. In urban flood events, long-term damage to land and property is caused by pollution from contaminated sediments left behind once the flood has subsided. Sediment particles can vary in size from clay and fine sand to gravel, large boulders and other debris, which can be entrained in strong flood flows. The transport processes are influenced by the particle size. Fine particles are usually entrained into suspension. Coarse particles are often transported as bedload, rolling or saltating along the bed.

*Correspondence to: Maggie J. Creed, School of Engineering, The University of Edinburgh, The King's Buildings, Edinburgh EH9 3JL, U.K.

Over the past twenty years, great progress has been made in developing coupled shallow water-sediment transport models for scenarios where either suspended sediment transport or bedload transport is dominant (see for example, [1, 4, 5, 6, 7]). An important conclusion from these advances is that it is imperative to use a non-capacity, fully-coupled water-sediment approach to obtain accurate results ([1, 2, 8, 9]). This is particularly the case when modelling rapidly-varying flow conditions over a mobile bed, such as when a dam break occurs. Many models presented in the literature to date use modified versions of the governing variable-density equations, where the variable-density term is manipulated out of the conserved-variable terms and redistributed into the source terms, increasing the complexity of the latter ([1]). Murillo *et al.* [10] proposed an augmented Roe solver for the variable-density shallow-water equations where this manipulation was avoided. The model is well-balanced and yields accurate results, even in the presence of a bed discontinuity. Recently, this model was extended by Juez *et al.* [6] to include suspended sediment transport but without bedload, where the hydrodynamic and suspended sediment equations are solved using finite volumes and the bathymetry is updated using a finite difference scheme.

Several finite-volume solvers have been developed for bedload transport only, where the conventional constant density shallow-water equations are coupled with an Exner-type bed morphological equation - with the latter incorporated into the Jacobian matrix of the complete system. This method is valid when the bedload discharge is expressed using a Grass-type formula, i.e. where a power of the flow velocity is multiplied by the Grass coefficient. Traditionally this coefficient is a constant and needs to be calibrated for each specific case, a limitation of this method. Murillo & Garcia Navarro [11] proposed a novel form of the Grass coefficient allowing it to be defined as a variable in a fully coupled model, thus extending the range of bedload formulae which can be used. However, determination of the eigenvalues for this system is complex and requires large computational effort. Following from [11], Juez *et al.* [12] presented a weakly-coupled model for bedload transport which reduced the computation time.

It is common for models which account for both suspended sediment and bedload transport to group the two processes into the same sediment flux equation (see for example [1, 3]). This is often done by modelling the sediment load as *total load*, and is justified because of the difficulty that exists in determining the transition between bedload transport and sediment transport under rapidly-varying flow conditions. However, the physical processes of bedload transport and suspended sediment are very different. Thus, it would be advantageous to have a numerical model that can be used easily either when one of the two processes dominates at a particular point in time or space, or if there is large variability in sediment size, because large, heavy particles are almost always transported as bedload while finer particles are easily entrained into suspension.

In light of these previous developments, here a new mathematical model is presented of the fully-coupled, unmanipulated, shallow water-sediment equations. The corresponding numerical model is solved on a uniform, Cartesian grid using a second-order Godunov-type finite-volume HLLC Riemann solver coupled with a MUSCL-Hancock time-integration scheme. The model considers both suspended sediment transport and bedload transport, and is an extension of the 1D model of Leighton *et al.* [5] and the 2D models of Apostolidou [13] and Jiang *et al.* [14]. The solution to the Riemann problem is derived following [15] and a generalised version of the HLLC contact wave speed estimate ([16]) is presented which accounts for the variable-density property.

The present shallow water-sediment flow model is first verified for the evolution of a sandbar by bedload transport. Semi-analytical solutions are presented for deposition of suspended sediment in the absence of entrainment, and entrainment without deposition. These solutions provide simple test cases to verify that a numerical model can simulate accurately the sediment flux exchange between the bed and the liquid-species mixture in the absence of complex flow dynamics. The well-balanced property of the solver is validated for a variable density dam break over a discontinuous bed. Finally the model is validated against laboratory-based data of a partial dam breach over a fixed bed, a numerical experiment of a complete dam break over a mobile bed which induces suspended sediment transport and against experimental data concerning a 2D partial dam breach flow over a mobile bed.

2. SHALLOW WATER-SEDIMENT EQUATIONS

2.1. Mathematical Model

The shallow water-sediment equations describe the flow of water-sediment mixtures in situations where horizontal length scales are much greater than the vertical water depth. Vertical particle acceleration is assumed to be negligible and the pressure is hydrostatic. Complete vertical mixing of the velocity and fluid density is also assumed when sediment is present in suspension. Hence, in shallow water-sediment models, the horizontal velocity component and the concentration of the suspended sediment are assumed to be homogeneous over the depth. The sediment is non reactive.

The shallow water-sediment equations are derived considering an infinitesimally thin element with dimensions, Δx and Δy , and water depth $h(i, j)$, where i and j are the cell indices in the x and y directions, respectively. The liquid-sediment mixture passes through the element with depth-

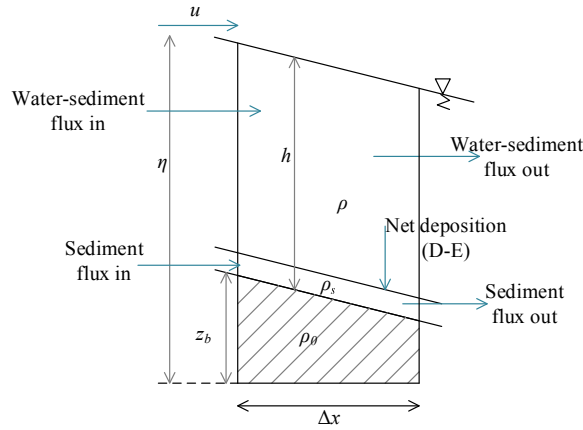


Figure 1. Control volume of bed and water sediment mixture.

integrated horizontal velocity components, $u(i, j)$ and $v(i, j)$. Following Yan [17], using principles of conservation of mass and momentum which consider fluxes of water-sediment mixture and sediment particles into and out of the control volume, and the overall sediment exchange with the bed, the five governing equations are derived by integrating over a control volume (Figure 1) in a small time interval Δt . This results in the following set of conservation laws for the conservation of mass and momentum (x and y directions) of the water-sediment mixture, conservation of mass of suspended sediment, and conservation of bedload and bed material:

$$\frac{\partial \rho h}{\partial t} + \frac{\partial \rho u h}{\partial x} + \frac{\partial \rho v h}{\partial y} = -\rho_0 \frac{\partial z_b}{\partial t} - \rho_s \frac{\partial q_{b_x}}{\partial x} - \rho_s \frac{\partial q_{b_y}}{\partial y}, \quad (1a)$$

$$\begin{aligned} \frac{\partial \rho u h}{\partial t} + \frac{\partial}{\partial x} \left(\rho u^2 h + \frac{1}{2} \rho g h^2 \right) + \frac{\partial \rho u v h}{\partial y} \\ = -\rho_s \frac{\partial q_{b_x}}{\partial t} - \rho_s \frac{\partial}{\partial x} (u_{b_x} q_{b_x}) - \rho g h \frac{\partial z_b}{\partial x} - \tau_{b_x}, \end{aligned} \quad (1b)$$

$$\begin{aligned} \frac{\partial \rho v h}{\partial t} + \frac{\partial}{\partial y} \left(\rho v^2 h + \frac{1}{2} \rho g h^2 \right) + \frac{\partial \rho u v h}{\partial x} \\ = -\rho_s \frac{\partial q_{b_y}}{\partial t} - \rho_s \frac{\partial}{\partial y} (u_{b_y} q_{b_y}) - \rho g h \frac{\partial z_b}{\partial y} - \tau_{b_y}, \end{aligned} \quad (1c)$$

$$\frac{\partial \rho_s h c}{\partial t} = -\frac{\partial(\rho_s h u c)}{\partial x} - \frac{\partial(\rho_s h v c)}{\partial y} - \rho_s (D - E), \quad (1d)$$

and

$$\frac{\partial z_b}{\partial t} = \frac{1}{(1 - \varepsilon)} \left(-\frac{\partial q_{bx}}{\partial x} - \frac{\partial q_{by}}{\partial y} + D - E \right), \quad (1e)$$

where h is the local depth of water-sediment mixture, ρ is the depth-averaged density of the water-sediment mixture, ρ_s is the density of the sediment, u and v are mean flow velocity components in the x and y directions, respectively, t is time, z_b is bed elevation, u_{bx} and u_{by} are bedload velocities, q_{bx} and q_{by} are bedload discharge components in the x and y directions, ε is bed porosity, g is acceleration due to gravity, and D and E are coefficients of deposition and entrainment fluxes representing the exchange of sediment between the bed and the liquid (discussed in greater detail in Section 2.2). The bed shear stress components, τ_{bx} and τ_{by} , are estimated from the following empirical expressions

$$\tau_{bx} = \rho c_f u \sqrt{u^2 + v^2}, \quad \text{and} \quad \tau_{by} = \rho c_f v \sqrt{u^2 + v^2}, \quad (2)$$

in which c_f is the dimensionless bed friction coefficient. The bed density is

$$\rho_0 = \rho_w \varepsilon + \rho_s (1 - \varepsilon), \quad (3)$$

where ρ_w is the density of clear water. The depth-averaged density of the water-sediment mixture, ρ , is a function of the depth-averaged sediment volumetric concentration, c , where

$$\rho = \rho_w + c(\rho_s - \rho_w). \quad (4)$$

Rearranging (4) we can write the concentration of suspended sediment as a function of the densities of water, sediment, and water-sediment mixture;

$$c = \frac{\rho - \rho_w}{\rho_s - \rho_w}. \quad (5)$$

In the absence of bedload transport, suspended sediment transport and bed morphological change, when the density of the liquid-species mixture is constant, equations (1a) - (1e) reduce to the classical shallow water equations of conservation of mass and momentum. The profile coefficients which arise from depth-averaging the governing equations are set to unity.

Equations (1a) to (1d) form a hyperbolic system of partial differential equations when written in the form,

$$\frac{\partial \mathbf{q}}{\partial t} + \frac{\partial \mathbf{f}}{\partial x} + \frac{\partial \mathbf{g}}{\partial y} = \mathbf{s}, \quad (6)$$

where,

$$\mathbf{q} = \begin{Bmatrix} \rho h \\ \rho u h \\ \rho v h \\ \rho_s c h \end{Bmatrix}, \quad \mathbf{f} = \begin{Bmatrix} \rho u h \\ \rho u^2 h + \frac{1}{2} \rho g h^2 \\ \rho u v h \\ \rho_s c u h \end{Bmatrix}, \quad \mathbf{g} = \begin{Bmatrix} \rho v h \\ \rho u v h \\ \rho v^2 h + \frac{1}{2} \rho g h^2 \\ \rho_s c v h \end{Bmatrix},$$

and,

$$\mathbf{s} = \begin{pmatrix} -\rho_0 \frac{\partial z_b}{\partial t} - \rho_s \frac{\partial q_{bx}}{\partial x} - \rho_s \frac{\partial q_{by}}{\partial y} \\ -\rho_s \frac{\partial q_{bx}}{\partial t} - \rho_s \frac{\partial}{\partial x}(u_{bx} q_{bx}) - \rho g h \frac{\partial z_b}{\partial x} - \tau_{bx} \\ -\rho_s \frac{\partial q_{by}}{\partial t} - \rho_s \frac{\partial}{\partial y}(u_{by} q_{by}) - \rho g h \frac{\partial z_b}{\partial y} - \tau_{by} \\ -\rho_s(D - E) \end{pmatrix}.$$

The above matrix system is solved using an approximate Riemann solver (see Section 3.2). The equation for updating the bed morphodynamics (1e), is solved using second-order central finite differences. The entire system is solved simultaneously at each time step, Δt .

2.2. Model Closure

To close the above system of equations, it is necessary to define parameters which describe the bed shear stresses, the sediment flux exchange between the bed layer and the liquid-sediment mixture, and the transport of material along the bed. Appropriate selection of empirical parameters is paramount for obtaining a physically relevant numerical solution. In the following test cases c_f , the dimensionless bed friction coefficient, is defined using the Manning equation such that

$$c_f = \frac{gn^2}{h^{1/3}}, \quad (7)$$

where, n is the Manning coefficient ($\text{sm}^{-1/3}$).

When the flow velocity exceeds a certain threshold value (see e.g. Soulsby [18]), sediment can be transported along the bed by rolling, saltating, or sliding of particles. This bedload transport is defined by the bedload discharge components, q_{bx} and q_{by} , and bedload particle velocity components, u_{bx} and u_{by} . If the flow velocity increases further and the shear velocity, u_* , exceeds the settling velocity of the particles, w_s , particles are entrained into suspension. Later, these particles can be deposited on the bed. Entrainment and deposition coefficients, E and D respectively, are used to express the processes which define this exchange of sediment between the bed and the liquid-sediment mixture. In the present work these parameters are described using well-established empirical formulae taken from the literature.

For the purpose of verifying the mathematical model presented above, the bedload discharge components are expressed with the widely used Meyer-Peter-Mueller (MPM) formula [19],

$$q_{bx} = 8\sqrt{(s-1)gd^3}(\theta_x - \theta_{cx})^{3/2}, \quad (8a)$$

$$q_{by} = 8\sqrt{(s-1)gd^3}(\theta_y - \theta_{cy})^{3/2}, \quad (8b)$$

where d is the median diameter of the sediment particle, $\theta_x = \frac{\tau_{bx}}{\rho(s-1)gd}$ and $\theta_{by} = \frac{\tau_{by}}{\rho(s-1)gd}$ are the components of the dimensionless shear stress (Shields parameter) in the x and y directions. The relative density of sediment $s = \rho_s/\rho$. The modified critical Shields parameters, θ_{cx} and θ_{cy} , are necessary to account for the influence that bed-slope can have on bedload transport, and are given by

$$\theta_{cx} = \theta_c \frac{\sin(\phi + \beta_x)}{\sin\beta_x}, \quad (9a)$$

$$\theta_{cy} = \theta_c \frac{\sin(\phi + \beta_y)}{\sin\beta_y}, \quad (9b)$$

where β_x and β_y represent the angles of the bed slope in the x and y directions, ϕ is the angle of repose of the sediment, and θ_c is the critical Shields parameter for the initiation of sediment transport on an horizontal bed.

Following Cao *et al.* ([1],[20]) we estimate the deposition and entrainment flux coefficients of suspended sediment from

$$D = w_s \alpha_d c (1 - \alpha_d c)^{m_d}, \quad (10)$$

and

$$E = \begin{cases} \alpha_e (\theta - \theta_c) u h^{-1} d^{-0.2} & \text{if } \theta \leq \theta_c, \\ 0 & \text{else,} \end{cases} \quad (11)$$

where m_d is an exponent, $\theta = \frac{\tau_b}{\rho(s-1)gd}$ is the local Shields parameter with the local bed shear stress, $\tau_b = \sqrt{\tau_{bx}^2 + \tau_{by}^2}$. For all of the following test cases, $\theta_c = 0.047$. The settling velocity of the sediment particles, w_s , is calculated using the well-established empirical formula of Zhang and Xie [21],

$$w_s = \sqrt{\left(\frac{13.95\nu}{d}\right)^2 + 1.09(s-1)gd - 13.95\frac{\nu}{d}}, \quad (12)$$

where ν is the kinematic viscosity and D_* is the dimensionless grain diameter,

$$D_* = \left(\frac{g(s-1)}{\nu^2}\right)d. \quad (13)$$

In equation (10), the coefficient α_d relates the depth-averaged concentration of suspended sediment c to the near-bed concentration and is given by,

$$\alpha_d = \min\left[2, \frac{1-\varepsilon}{c}\right]. \quad (14)$$

The coefficient α_e in equation (11) is a function of grain diameter, sediment density, bed porosity, and critical Shields parameter, and has to be calibrated for each specific case.

The Rouse number, R_n , is used to determine whether the transport process is predominantly bedload or suspended sediment transport, or a combination of both. It is defined as

$$R_n = \frac{w_s}{\kappa u_*},$$

where w_s is the settling velocity of an individual sediment particle, $\kappa = 0.4$, is the von Kármán constant. The dominant transport process is selected by implementing the condition,

$$R_n \geq 2.5 \quad \text{bedload only,}$$

$$1.2 \leq R_n < 2.5 \quad \text{suspended sediment and bedload,}$$

$$R_n < 1.2 \quad \text{suspended sediment only.}$$

When both suspended sediment and bedload transport are present, R_n is used, combined with a simple weighted distribution, to estimate the percentage of sediment transported by each mode. For example, if $\kappa R_n \approx 0.9$, it is assumed that 80% of the sediment is transported as bedload and 20% as suspended load. Similarly, if $\kappa R_n \approx 0.6$, 20% is attributed to bedload transport and the remainder transported as suspended sediment. The importance of using the Rouse number to obtain accurate results is demonstrated in Section 6.2.

The foregoing empirical formulae have been derived for case-specific values of bed friction and resulting shear stress. Closure relationships are often derived from experimental data for cases of low shear stress ([1]). For practical applications, a calibration study is necessary when selecting the appropriate formulations and corresponding empirical coefficients prior to applying the model.

3. NUMERICAL SCHEME

3.1. Finite Volume solver

A Godunov-type finite volume Riemann solver is used to solve equation (6) on a uniform grid. The solver, which is second-order accurate in space, is robust, conservative, and preserves shocks and discontinuities, such as those which can occur in the free surface or velocity gradients induced by dam breach flow. MUSCL-Hancock time integration combined with a slope limiter is used to ensure the solution is second-order accurate in time.

The hyperbolic system of conservation laws given by (6) is expressed as a volume integral,

$$\frac{\partial}{\partial t} \int_{\Omega} \mathbf{q} d\Omega + \int_{\Omega} \frac{\partial \mathbf{f}}{\partial x} d\Omega + \int_{\Omega} \frac{\partial \mathbf{g}}{\partial y} d\Omega = \int_{\Omega} \mathbf{s} d\Omega. \quad (15)$$

In Cartesian form we can write the solution at the centre of each cell,

$$\mathbf{q}_{i,j}^{k+1} = \mathbf{q}_{i,j}^k - \frac{\Delta t}{\Delta x} (\mathbf{f}_{i+1/2,j} - \mathbf{f}_{i-1/2,j}) - \frac{\Delta t}{\Delta y} (\mathbf{g}_{i,j+1/2} - \mathbf{g}_{i,j-1/2}) + \Delta t \mathbf{s}_{i,j}, \quad (16)$$

where $\mathbf{f}_{i+1/2,j}$, $\mathbf{f}_{i-1/2,j}$, $\mathbf{g}_{i,j+1/2}$ and $\mathbf{g}_{i,j-1/2}$ are the fluxes passing through the east, west, north and south faces of the cell, respectively. Δx and Δy are the cell dimensions in the x and y directions. $\mathbf{q}_{i,j}$ and $\mathbf{s}_{i,j}$ are the vectors of the dependent variables and source terms. The fluxes and source terms are evaluated at time step $k + 1$ but the superscript has been left out for simplicity.

3.2. Variable density Riemann problem

An HLLC approximate Riemann solver (see e.g. Fraccarollo and Toro [22]) is used to solve (15). A complete description of this method is given by Toro *et al.* [15]. One of the major advantages of the HLLC scheme, expanded from the earlier HLL (Harten Lax and Leer [23]) Riemann problem by [15], is that it can account for intermediate contact waves (S_* in Figure 2), for example those which arise in the case of 2D flow over a dry bed, or a discontinuity in the mixture density. No specific wetting or drying algorithm is used in the current numerical model.

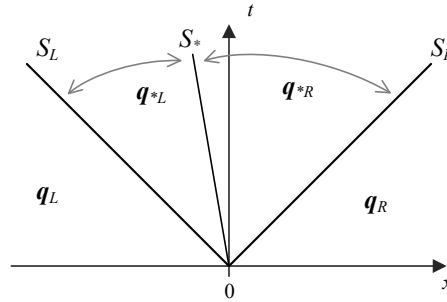


Figure 2. HLLC of the Riemann problem with S_L , S_* and S_R describing the wave speeds of the left, contact (middle) and right waves.

By analysing the eigenstructure of the conventional shallow water equations, Fraccarollo and Toro [22] showed that the normal velocity component and the water depth remain constant through the contact wave S_* , and only the tangential velocity changes. It will be demonstrated that the property of constant normal velocity holds across the contact wave for the variable-density equations. However, across the contact wave associated with a discontinuity in mixture density, the water depth can vary and is determined by the mixture density. Moreover, it will be shown that the density of the water-sediment mixture is constant across rarefaction and shock waves. Similarly to Fraccarollo and Toro [22], the solution to the Riemann problem is derived by determining the Jacobian matrix

and eigenvalues and eigenvectors of system (15) and then solving the Riemann invariants across the continuous waves and the Rankine-Hugoniot conditions across the shock waves.

At this point it is important to note that equation (6) is valid only for smoothly varying bathymetry, i.e. it cannot model shallow flow at a vertical bed step or a hydraulic jump formed at a steep slope exactly. In this section the HLLC solver will be presented for (6) and then extended to allow for a discontinuous bathymetry in Section 4.1.

3.3. Eigenvalue problem

The Jacobian matrix and the corresponding eigenstructure of the variable-density problem differ from the conventional shallow water problem and also from the formulation of the variable-density problem proposed by Cao *et al.* [1], in which the variable-density term ρ is eliminated from the conserved variables of the water-sediment mixture mass and momentum equations and redistributed to the source terms. The Jacobian matrix \mathbf{C} is an extension of the 1D problem presented by Leighton *et al.* [5] and is similar to the Jacobian matrix given by Murillo *et al.* [10],

$$\mathbf{C} = \begin{bmatrix} 0 & n_x & n_y & 0 \\ (a^2 - u^2 + \alpha)n_x - uvn_y & 2un_x + vn_y & un_y & -\beta n_x \\ -uvn_x + (a^2 - u^2 + \alpha)n_y & vn_x & un_x + 2vn_y & -\beta n_y \\ -\frac{\rho_s c}{\rho}(un_x + vn_y) & \frac{\rho_s c}{\rho}n_x & \frac{\rho_s c}{\rho}n_y & un_x + vn_y \end{bmatrix},$$

where the local dynamic wave velocity, $a = \sqrt{gh}$, and coefficients,

$$\alpha = \frac{(\rho_s - \rho_w)ca^2}{2\rho_w} \quad \text{and} \quad \beta = \frac{(\rho_s - \rho_w)\rho a^2}{2\rho_s \rho_w}.$$

The vector of eigenvalues of the combined system is found to be

$$\begin{Bmatrix} \lambda_1 \\ \lambda_2 \\ \lambda_3 \\ \lambda_4 \end{Bmatrix} = \begin{bmatrix} un_x + vn_y - a \\ un_x + vn_y \\ un_x + vn_y + a \\ un_x + vn_y \end{bmatrix}. \quad (17)$$

Since the 2D Riemann problem is treated as two 1D problems applied in the x and y directions, the solution across the rarefaction, shock and shear waves shall be presented in the x direction only. Letting $n_x = 1$, the corresponding Jacobian, $\mathbf{A}(\mathbf{q})$, of the *quasi-linear* system,

$$\mathbf{q}_t + \mathbf{A}(\mathbf{q})\mathbf{q}_x = \mathbf{s}, \quad (18)$$

is

$$\mathbf{A}(\mathbf{q}) = \begin{bmatrix} 0 & 1 & 0 & 0 \\ (a^2 - u^2 + \alpha) & 2u & 0 & -\beta \\ -uv & v & u & 0 \\ -\frac{\rho_s c}{\rho}u & \frac{\rho_s c}{\rho} & 0 & u \end{bmatrix},$$

where \mathbf{q}_t is the derivative of the matrix of conserved variables with respect to time, \mathbf{q}_x is the derivative of the matrix of conserved variables with respect to x and \mathbf{s} is the matrix of source terms in the x direction. The absolute values of the eigenvalues are

$$\begin{Bmatrix} \lambda_1 \\ \lambda_2 \\ \lambda_3 \\ \lambda_4 \end{Bmatrix} = \begin{bmatrix} u - a \\ u \\ u + a \\ u \end{bmatrix}. \quad (19)$$

Vector (19) is similar to that of the constant-density 2D shallow-water problem, noting that the present variable-density problem is hyperbolic, but not strictly hyperbolic, since one of the eigenvalues has a multiplicity of 2; $\lambda_2 = \lambda_4 = u$.

3.4. Properties of the HLLC wave structure

The Riemann problem is now solved in a similar way to the conventional shallow-water problem (Toro [16]), by analysing the Rankine-Hugoniot condition across the shock waves and considering the generalised Riemann invariants across the rarefaction and shear waves using the right eigenvector of the Jacobian matrix;

$$\mathbf{R} = \begin{bmatrix} 1 & 0 & 1 & \frac{\rho(\rho_s - \rho_w)}{\rho_s(\rho_w + \rho)} \\ u - a & 0 & u + a & u \frac{\rho(\rho_s - \rho_w)}{\rho_s(\rho_w + \rho)} \\ v & 1 & v & 0 \\ \frac{\rho_s c}{\rho} & 0 & \frac{\rho_s c}{\rho} & 1 \end{bmatrix}.$$

For a left rarefaction, consider the Riemann invariants of $\mathbf{R}^{(1)}$,

$$\frac{d\rho h}{1} = \frac{d\rho u h}{u - a} = \frac{d\rho v h}{v} = \frac{d\rho_s h}{\rho_s c / \rho}. \quad (20)$$

Equating the first and last terms of (20), it is found that the following properties hold across the left rarefaction (see Appendix A);

$$\rho = \text{constant}, \quad c = \text{constant}, \quad v = \text{constant} \quad \text{and} \quad u + 2a = \text{constant}. \quad (21)$$

Similar considerations across the right rarefaction using $\mathbf{R}^{(3)}$ yield,

$$\rho = \text{constant}, \quad c = \text{constant}, \quad v = \text{constant} \quad \text{and} \quad u - 2a = \text{constant}. \quad (22)$$

For a shock wave, the Rankine-Hugoniot condition holds such that

$$\mathbf{f}(\mathbf{q}_{*L}) - \mathbf{f}(\mathbf{q}_L) = \mathbf{S}_L(\mathbf{q}_{*L} - \mathbf{q}_L) \quad \text{for a left shock wave}, \quad (23)$$

$$\mathbf{f}(\mathbf{q}_R) - \mathbf{f}(\mathbf{q}_{*R}) = \mathbf{S}_R(\mathbf{q}_R - \mathbf{q}_{*R}) \quad \text{for a right shock wave}, \quad (24)$$

where S_L and S_R are the speeds of the left and right shock waves respectively, and subscripts $L, *L, R$ and $*R$ denote the states of the Riemann problem as shown in Figure 2. Application of equations (23) and (24) to Equation (6) (see Appendix A for details) verifies that the tangential velocity across a shock wave is constant, as expected following from the constant-density problem, i.e.,

$$\hat{v}_{*L} = \hat{v}_L, \quad (25)$$

Moreover, it is verified that the density of the water-sediment mixture is preserved across the shock wave such that,

$$\rho_L = \rho_{*L}, \quad (26)$$

This mathematical derivation demonstrates consistency with the physical assumption made when deriving the governing equations; that the suspended sediment particles are carried at the same speed as the water particles. Thus, the presence of sediment does not impact the properties of the flow velocity and water depth across shock waves and rarefaction waves.

In summary, across a shock wave,

$$\rho_{*L} = \rho_L, \quad \rho_{*R} = \rho_R, \quad (27)$$

$$c_{*L} = c_L, \quad c_{*R} = c_R, \quad (28)$$

$$v_{*L} = v_L, \quad v_{*R} = v_R. \quad (29)$$

Across the shear wave, or contact discontinuity, using $\mathbf{R}^{(2)}$ or $\mathbf{R}^{(4)}$ it is shown that (see Appendix A for details)

$$\rho_{*L} h_{*L}^2 = \rho_{*R} h_{*R}^2 = \rho_* h_*^2, \quad (30)$$

$$u_{*L} = u_{*R} = S_*, \quad (31)$$

$$v_{*L} \neq v_{*R} \quad \text{for } \mathbf{R}^{(2)}, \quad (32)$$

$$v_{*L} = v_{*R} \quad \text{for } \mathbf{R}^{(4)}. \quad (33)$$

From Equation (30), it is clear that the depth of the fluid must change across a contact discontinuity associated with a jump in fluid density. This will be verified numerically in Sections 5.5 and 6.2. The properties defined in Equations (21) to (33) are now used to solve approximately the Riemann problem using the HLLC approach, similar to Toro [16].

Letting $u_* = S_*$, the Rankine-Hugoniot condition across the left and right shock waves gives,

$$(\rho h^2)_{*L} = -\frac{\rho_L h_L^2 (S_L - u_L)}{(S_* - S_L)}, \quad (34)$$

and

$$(\rho h^2)_{*R} = -\frac{\rho_R h_R^2 (S_R - u_R)}{(S_* - S_R)}. \quad (35)$$

Following from condition (30), equating (34) and (35) such that,

$$\rho_R h_R^2 (S_R - u_R) (S_* - S_R) = \rho_L h_L^2 (S_L - u_L) (S_* - S_R), \quad (36)$$

the equation for the middle wave speed S_* is obtained;

$$S_* = \frac{S_L \rho_R h_R^2 (S_R - u_R) - S_R \rho_L h_L^2 (S_L - u_L)}{\rho_R h_R^2 (S_R - u_R) - \rho_L h_L^2 (S_L - u_L)}. \quad (37)$$

This is very similar to the solution of S_* obtained for the classic shallow-water equations presented by Toro [16]. The main difference is that here, the variable depth-integrated mass of the water-sediment mixture, ρh , must be incorporated when calculating S_* . Equation (37) is a generalised form of the equation given by Toro [16]. When ρ is constant in space and time, (37) reduces to the equation for S_* proposed by [16]. For the examples considered in this paper, a similar result is obtained when using either Equation (37) or the equation for the middle wave given by Toro [16]. However, the results could be expected to differ for a highly concentrated bore of water-sediment mixture flowing into a region of clear water, such as a mud flow entering a lake or a tsunami front in the form of a broken wave.

The approximate solution to the numerical flux, $\mathbf{f}_{i+\frac{1}{2}}$, at the interface between two adjacent grid cells can now be calculated as

$$\mathbf{f}_{i+\frac{1}{2}, j} = \begin{cases} \mathbf{f}_L & \text{if } 0 \leq S_L \\ \mathbf{f}_{*L} & \text{if } S_L \leq 0 \leq S_* \\ \mathbf{f}_{*R} & \text{if } S_* \leq 0 \leq S_R \\ \mathbf{f}_R & \text{if } 0 \geq S_R \end{cases}$$

where $\mathbf{f}_L = \mathbf{f}(\mathbf{q}_L)$ and $\mathbf{f}_R = \mathbf{f}(\mathbf{q}_R)$ are calculated from the left and right Riemann states, \mathbf{q}_L and \mathbf{q}_R , respectively. The fluxes to the left and right of the contact wave, \mathbf{f}_{*L} and \mathbf{f}_{*R} , are given by

$$\mathbf{f}_{*L} = \begin{bmatrix} f_{*1} \\ f_{*2} \\ v_L f_{*1} \\ \frac{\rho_s c_L}{\rho_L} f_{*1} \end{bmatrix} \quad \text{and} \quad \mathbf{f}_{*R} = \begin{bmatrix} f_{*1} \\ f_{*2} \\ v_R f_{*1} \\ \frac{\rho_s c_R}{\rho_R} f_{*1} \end{bmatrix},$$

where the fluxes, f_{*1} and f_{*2} are the HLL flux components calculated using the vector equation ([23])

$$\mathbf{f}_* = \frac{S_R \mathbf{f}_L - S_L \mathbf{f}_R + S_L S_R (\mathbf{q}_R - \mathbf{q}_L)}{S_R - S_L}.$$

Values of the left and right wave speeds for the two wave Riemann problem, S_L and S_R , are estimated following Fraccarollo and Toro [22] as:

$$S_L = \begin{cases} u_R - 2\sqrt{gh_R} & \text{if } h_L = 0 \\ \min(u_L - \sqrt{gh_L}, u_* - \sqrt{gh_*}) & \text{if } h_L > 0 \end{cases},$$

and

$$S_R = \begin{cases} u_L + 2\sqrt{gh_L} & \text{if } h_R = 0 \\ \max(u_R + \sqrt{gh_R}, u_* + \sqrt{gh_*}) & \text{if } h_R > 0 \end{cases},$$

where u_L , u_R , h_L and h_R are the left and right constant Riemann states and the velocity and water depth in the star region, u_* and h_* are given by

$$u_* = \frac{1}{2}(u_L + u_R) + \sqrt{gh_L} - \sqrt{gh_R}, \quad (38)$$

and

$$h_* = \frac{1}{g} \left[\frac{1}{2}(\sqrt{gh_L} + \sqrt{gh_R}) + \frac{1}{4}(u_L - u_R) \right]^2. \quad (39)$$

Unlike the four equations of system (6) solved above, in its general form, the bed morphological equation (1e) is not a traditional advection equation. Some authors (see e.g. [24], [11], [25]) have solved Equation (1e) using finite volumes by including it in the above eigenvalue problem. However, this is only valid for subcritical and supercritical flows when a Grass-type bedload formula is used to estimate the bedload discharge. To ensure that the model can be extended and applied to a wider range of physical scenarios while avoiding additional computational effort (as required in [11]), here the bed morphological equation (1e) is calculated using second-order central differences. The system of equations is still defined as a fully coupled model because the bed morphological equation and Equation (6) are simultaneously updated at each time step.

The source terms are evaluated at the centre of the grid cells, also using second-order accurate central differences. Verification and validation tests will show that this is an acceptably accurate method for updating the source terms for the engineering applications considered here.

It has been noted in Section 3.2 that the water depth-discharge form of the shallow water-sediment equations (1) is valid for a smoothly varying bathymetry. Although much of the laboratory based data available in the literature to validate shallow water-sediment models lie within this category, if the bed exhibits a sharp discontinuity, Equation (1) cannot account for the pressure change at the bed step and spurious oscillations develop in the free surface elevation profile (see for example, Rogers *et al.* [26]). This is because the surface gradient terms in the momentum equations (1b) and (1c) are split between the pressure flux gradient term and the source term which accounts for the bed slope. Various numerical and mathematical balancing techniques exist in the literature (see e.g. [27, 28, 29, 30]). Here, an algebraic balancing technique is employed, based on a similar approach used by Liang and Borthwick [31], to prevent such instabilities arising. This avoids the need to implement a numerical balancing technique, which can increase the complexity of the numerical scheme.

4. WELL-BALANCED EQUATIONS

4.1. Balancing the Shallow Water-Sediment Equations

Letting the water depth, $h = \eta - z_b$, where η is the free surface elevation above a given datum, following a similar approach to Liang and Borthwick [31] Equation (1) is rewritten as,

$$\frac{\partial \rho \eta}{\partial t} + \frac{\partial \rho u h}{\partial x} + \frac{\partial \rho v h}{\partial y} = -\rho_0 \frac{\partial z_b}{\partial t} - \rho_s \frac{\partial q_{b_x}}{\partial x} - \rho_s \frac{\partial q_{b_y}}{\partial y} + \frac{\partial \rho z_b}{\partial t}, \quad (40a)$$

$$\begin{aligned} \frac{\partial \rho u h}{\partial t} + \frac{\partial}{\partial x} \left(\rho u^2 h + \frac{1}{2} \rho g (\eta^2 - 2\eta z_b) \right) + \frac{\partial \rho u v h}{\partial y} \\ = -\rho_s \frac{\partial q_{b_x}}{\partial t} - \rho_s \frac{\partial}{\partial x} (u_{b_x} q_{b_x}) - \rho g \eta \frac{\partial z_b}{\partial x} + \frac{1}{2} g z_b^2 \frac{\partial \rho}{\partial x} - \tau_{b_x}, \end{aligned} \quad (40b)$$

$$\begin{aligned} \frac{\partial \rho v h}{\partial t} + \frac{\partial}{\partial y} \left(\rho v^2 h + \frac{1}{2} \rho g (\eta^2 - 2\eta z_b) \right) + \frac{\partial \rho u v h}{\partial x} \\ = -\rho_s \frac{\partial q_{b_y}}{\partial t} - \rho_s \frac{\partial}{\partial y} (u_{b_y} q_{b_y}) - \rho g \eta \frac{\partial z_b}{\partial y} + \frac{1}{2} g z_b^2 \frac{\partial \rho}{\partial y} - \tau_{b_y}, \end{aligned} \quad (40c)$$

$$\frac{\partial \rho_s h c}{\partial t} = -\frac{\partial (\rho_s h u c)}{\partial x} - \frac{\partial (\rho_s h v c)}{\partial y} - \rho_s (D - E), \quad (40d)$$

and

$$\frac{\partial z_b}{\partial t} = \frac{1}{(1 - \varepsilon)} \left(-\frac{\partial q_{b_x}}{\partial x} - \frac{\partial q_{b_y}}{\partial y} + D - E \right). \quad (40e)$$

System (40) is now well-balanced since the pressure terms of the momentum equations are implicitly balanced in the mathematical formulation. The advantage of using the well-balanced equations is that the numerical model is now more generally applicable than (1), as demonstrated in Figure 7, without the need for additional complex numerical balancing techniques.

4.2. Convenient form of the governing equations

To simplify the numerical scheme and solve the governing equations (40) simultaneously at each time step, the dependent variables, ρ , η (or h when system (1) is used), c , u and v in Equations (40a)-(40d) are substituted for by new variables, M , p_x , p_y , and M_S , following the approach of Apostolidou [13].

Let,

$$M = \rho \eta, \quad p_x = \rho u h, \quad p_y = \rho v h, \quad \text{and} \quad M_S = \rho_s c h, \quad (41)$$

where M incorporates the mass of the liquid-sediment mixture, p_x and p_y are momenta of the liquid-sediment mixture in the x and y directions, and M_S is the depth integrated mass of suspended sediment.

Substituting for the above variables (40a)-(40d) can be rewritten as

$$\frac{\partial M}{\partial t} + \frac{\partial p_x}{\partial x} + \frac{\partial p_y}{\partial y} = -\rho_0 \frac{\partial z_b}{\partial t} - \rho_s \frac{\partial q_{b_x}}{\partial x} - \rho_s \frac{\partial q_{b_y}}{\partial y} + \frac{\partial \rho z_b}{\partial t}, \quad (42a)$$

$$\begin{aligned}
& \frac{\partial p_x}{\partial t} + \frac{\partial}{\partial x} \left(p_x u + \frac{1}{2} g \frac{M^2}{\rho} - g z_b M \right) + \frac{\partial p_x v}{\partial y} \\
& = -\rho_s \frac{\partial q_{b_x}}{\partial t} - \rho_s \frac{\partial}{\partial x} (u_{b_x} q_{b_x}) - \rho g \eta \frac{\partial z_b}{\partial x} + \frac{1}{2} g z_b^2 \frac{\partial \rho}{\partial x} - \tau_{b_x},
\end{aligned} \tag{42b}$$

$$\begin{aligned}
& \frac{\partial p_y}{\partial t} + \frac{\partial}{\partial y} \left(p_y v + \frac{1}{2} g \frac{M^2}{\rho} - g z_b M \right) + \frac{\partial p_y u}{\partial x} \\
& = -\rho_s \frac{\partial q_{b_y}}{\partial t} - \rho_s \frac{\partial}{\partial y} (u_{b_y} q_{b_y}) - \rho g \eta \frac{\partial z_b}{\partial y} + \frac{1}{2} g z_b^2 \frac{\partial \rho}{\partial y} - \tau_{b_y}.
\end{aligned} \tag{42c}$$

and

$$\frac{\partial M_S}{\partial t} = -\frac{\partial M_S u}{\partial x} - \frac{\partial M_S v}{\partial y} - \rho_s (D - E), \tag{42d}$$

The components of the hyperbolic system (6), solved using the HLLC solver described in Section 3.1 are now given by,

$$\mathbf{q} = \begin{Bmatrix} M \\ p_x \\ p_y \\ M_S \end{Bmatrix}, \quad \mathbf{f} = \begin{Bmatrix} p_x u + \frac{1}{2} g \frac{M^2}{\rho} - g z_b M \\ p_y u \\ M_S u \end{Bmatrix}, \quad \mathbf{g} = \begin{Bmatrix} p_y v + \frac{1}{2} g \frac{M^2}{\rho} - g z_b M \\ M_S v \end{Bmatrix},$$

and

$$\mathbf{s} = \begin{Bmatrix} -\rho_0 \frac{\partial z_b}{\partial t} - \rho_s \frac{\partial q_{b_x}}{\partial x} - \rho_s \frac{\partial q_{b_y}}{\partial y} + \frac{\partial \rho z_b}{\partial t} \\ -\rho_s \frac{\partial q_{b_x}}{\partial t} - \rho_s \frac{\partial}{\partial x} (u_{b_x} q_{b_x}) - \rho g \eta \frac{\partial z_b}{\partial x} + \frac{1}{2} g z_b^2 \frac{\partial \rho}{\partial x} - \tau_{b_x} \\ -\rho_s \frac{\partial q_{b_y}}{\partial t} - \rho_s \frac{\partial}{\partial y} (u_{b_y} q_{b_y}) - \rho g \eta \frac{\partial z_b}{\partial y} + \frac{1}{2} g z_b^2 \frac{\partial \rho}{\partial y} - \tau_{b_y} \\ -\rho_s (D - E) \end{Bmatrix}.$$

Rogers *et al.* [26] showed that the Jacobian matrix and the eigenstructure of the balanced shallow water equations are the same as the unbalanced equations for the constant density case. For the variable density equations presented here, the Jacobian matrix of (40) is not identical to that of (1). However, since balancing does not change the wave speeds of the physical variables, here we assume that the eigenvalues of system (40) are the same as those of (1). As a result, the wave speeds derived in Section 3.2 above are retained in the HLLC solver of Equation (42). The relationships defined in (41) are then used to find updated values of the conserved variables. The validity of this assumption is investigated in Section 6.2.

4.3. Boundary Conditions

In the majority of the cases presented here, two simple boundary conditions are applied: closed, slip conditions; or open, transmissive conditions. Slip conditions represent a frictionless, reflective solid boundary where the velocity normal to the wall is zero and the tangential flow along the wall is unrestrained. If the solid boundary is running in the x direction,

$$M_B^{k+1} = M_I^{k+1}, \quad p_{xB}^{k+1} = -p_{xI}^{k+1}, \quad p_{yB}^{k+1} = p_{yI}^{k+1}, \tag{43}$$

$$M_S^{k+1} = M_{S_I}^{k+1}, \quad z_{bB}^{k+1} = z_{bI}^{k+1},$$

where B represents the cell outside the domain boundary, I is the cell inside the domain boundary and k is the k^{th} timestep.

Transmissive, or open, boundary conditions are applied to allow inflow to and outflow from the domain.

$$M_B^{k+1} = M_I^{k+1}, \quad p_{xB}^{k+1} = p_{xI}^{k+1}, \quad p_{yB}^{k+1} = p_{yI}^{k+1}, \quad (44)$$

$$M_S^{k+1} = M_{S_I}^{k+1}, \quad z_{bB}^{k+1} = z_{bI}^{k+1}.$$

Grid and time step convergence tests have been carried out for every test case to obtain a sensible balance between accuracy and computational efficiency.

5. VERIFICATION AGAINST SEMI-ANALYTICAL SOLUTIONS

5.1. Bedload: Evolution of a 1D sandbar in steady flow

This test is used to verify that the solver is capable of modelling bedload transport and bed morphodynamic change. It is a 2D simulation analogous to the 1D test case presented by Hudson and Sweby [24] to predict the evolution of a sandbar along a flat frictionless, non-erodible bed in an open channel. The case was subsequently modelled by other researchers including Castro Diaz *et al.* [4], Huang *et al.* [32] and Zhou [7]. An approximate analytical solution for the bed morphology was developed by [24] following De Vries [33]. The problem domain consists of a frictionless channel of plan dimensions length 1000 m x width 240 m. The initial horizontal bed is flat everywhere, except for a 1 m high hump located between $x_1 = 300$ m and $x_2 = 500$ m. The initial conditions for flow depth h , bed elevation z_b , and flow velocity u are:

$$h(x, t_0) = 10.0 \text{ m} - z_b(x, t_0), \quad (45)$$

$$z_b(x, t_0) = \begin{cases} z_{bmax} \sin^2\left(\frac{\pi(x-x_1)}{(x_2-x_1)}\right) \text{ m} & \text{if } 300 \text{ m} \leq x \leq 500 \text{ m}, \\ 0 & \text{otherwise,} \end{cases}$$

and

$$u(x, t_0) = \frac{q_0}{h(x, t_0)}, \quad (46)$$

where z_{bmax} is the maximum initial height of the hump and $q_0 = 10 \text{ m}^3\text{s}^{-1}$ is the initial flow discharge. The bedload flux, q_b , is calculated using Meyer-Peter-Mueller formula (8). The porosity of the bed $\varepsilon = 0.4$. **For a bed composed of coarse grains, $R_n \gg 2.5$ under the flow conditions given above, i.e. bedload transport dominates, and so suspended sediment, deposition and entrainment processes are set to zero.**

For $m = 3$, $\eta = 10 \text{ m}$ and $A = 0.01 \text{ s}^2\text{m}^{-1}$, the approximate analytical solution presented by [24] is valid until $t \approx 23800 \text{ s}$.

The numerical grid comprises 400 cells in the x -direction, such that $\Delta x = 2.5 \text{ m}$, and 5 cells in the y -direction, such that $\Delta y = 5 \text{ m}$. The time step $\Delta t = 0.1 \text{ s}$.

The model is initially run for approximately 40,000 s with the bed fixed, until a steady-state flow field is achieved. The model is then run for 33,000 s for a mobile bed. Since no exact analytical solution exists for this problem, the numerical results are compared to the approximate analytical solution given by Hudson and Sweby [24] where it is assumed that the flow discharge and the free surface elevation remain constant throughout the whole domain.

Figure 3 shows the numerical model results are in satisfactory agreement with the approximate analytical solution. As the sandbar propagates along the bed (Figure 4), the downstream face

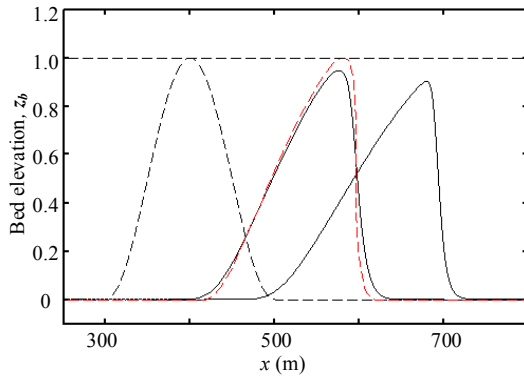


Figure 3. Bed hump profile at $t = 0$ (dashed black line), analytical solution at $t/T = 11.9$ (dashed red line) and the numerical results (solid black line) at $t = 23800$ s and 33000 s.

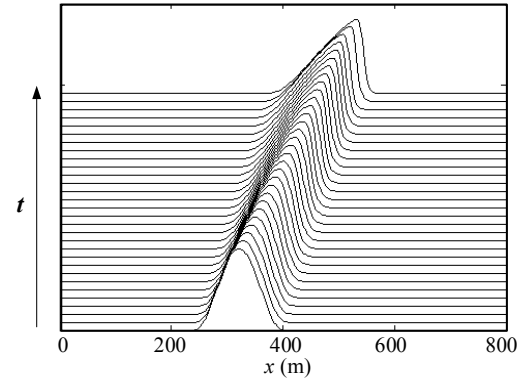


Figure 4. Stacked $x - t$ plots of evolution of the hump from $t = 0$ until $t = 33000$ s.

steepens, eventually forming a vertical shock after $t \approx 23800$ s, after which time the analytical solution is no longer valid. However, as seen in Figure 3, the numerical model is valid for all $t > 0$ s. Use of the modified critical Shields parameter from Equation (9) prevents any non-physical oscillations forming in the bed profile which can occur when using a finite difference solver for the bed morphological equation (40e) (e.g. [32]), because it allows for the diffusion which occurs naturally in bedload transport on steep-sloping beds (e.g. Soulsby [18]).

5.2. Suspended Sediment

To verify the model's capability to simulate accurately the deposition and entrainment of suspended sediment, simple semi-analytical solutions are derived following a similar approach to that of Apostolidou [13]. Two cases are presented below: deposition in the absence of entrainment; and entrainment with no deposition. In both cases, the problem consists of a flat-bottomed rectangular tank with a fixed free surface elevation. There is no net horizontal flow but there is intense mixing in the vertical direction, corresponding to a homogeneous water-sediment solution for the depth of the tank. Bedload transport is neglected. Making the foregoing assumptions, after some rearranging Equations (1) simplify to give

$$\frac{\partial h}{\partial t} + \frac{\partial hu}{\partial x} + \frac{\partial hv}{\partial y} = \frac{E - D}{(1 - \varepsilon)}, \quad (47a)$$

$$\begin{aligned} \frac{\partial(uh)}{\partial t} + \frac{\partial}{\partial x}(u^2h + \frac{1}{2}gh^2) + \frac{\partial uvh}{\partial y} \\ = -gh \frac{\partial z_b}{\partial x} - \tau_{bx} - \frac{(\rho_s - \rho_w)}{2\rho} gh^2 \frac{\partial c}{\partial x} - \frac{(\rho_0 - \rho)(E - D)u}{\rho(1 - \varepsilon)}, \end{aligned} \quad (47b)$$

$$\begin{aligned} \frac{\partial vh}{\partial t} + \frac{\partial}{\partial y}(v^2h + \frac{1}{2}gh^2) + \frac{\partial uvh}{\partial x} \\ = -gh \frac{\partial z_b}{\partial y} - \tau_{by} - \frac{(\rho_s - \rho_w)}{2\rho} gh^2 \frac{\partial c}{\partial y} - \frac{(\rho_0 - \rho)(E - D)v}{\rho(1 - \varepsilon)}, \end{aligned} \quad (47c)$$

$$\frac{\partial hc}{\partial t} = -\frac{\partial huc}{\partial x} - \frac{\partial hvc}{\partial y} - \rho_s(D - E), \quad (47d)$$

and

$$\frac{\partial z_b}{\partial t} = \frac{1}{(1 - \varepsilon)} (D - E) . \quad (47e)$$

In a tank with a horizontal bed and a horizontal free surface, the governing equations further reduce to

$$\frac{\partial h}{\partial t} = \frac{E - D}{(1 - \varepsilon)} , \quad (48a)$$

$$\frac{\partial c}{\partial x} = \frac{\partial c}{\partial y} = 0 , \quad (48b)$$

$$\frac{\partial(hc)}{\partial t} = E - D \quad (48c)$$

and

$$\frac{\partial z_b}{\partial t} = \frac{D - E}{(1 - \varepsilon)} . \quad (48d)$$

5.3. Deposition in flat-bottomed tank of still water with no entrainment

For deposition of dilute suspended sediment in a flat-bottomed tank with no net flow and no entrainment but intense vertical mixing, $u = 0$, $E = 0$, $\tau_b = 0$, and $D = cw_s$. Assuming that the solution is in the form $c = c_0 e^{-t/T}$ for any time $0 \leq t \leq \infty$, where T is a characteristic time constant, then

$$h = h_0 - \frac{c_0 h_0}{(1 - \varepsilon - c_0)} (e^{-t/T} - 1), \quad (49)$$

and

$$z_b = z_{b0} + \frac{c_0 h_0}{(1 - \varepsilon - c_0)} (e^{-t/T} - 1), \quad (50)$$

where

$$T = \frac{h_0}{w_s \left(1 - \frac{1}{(1 - \varepsilon)} c_0 \right)} . \quad (51)$$

In the above equation, h_0 , z_{b0} , and c_0 are initial values for the water depth, the bed elevation above a fixed horizontal datum and the concentration of suspended sediment (at time $t = 0$). h , z_b and c are the water height, bed elevation and concentration of suspended sediment at any time, $t > 0$. In the numerical model, the initial free surface water elevation and bed elevation are 6 m and 1 m above the datum, respectively. The numerical model is run for 5000 s with an initial concentration of suspended sediment equal to 0.5 %. Figure 5 depicts the time histories of the bed elevation, water depth and elevation of the free surface. The majority of the sediment settles out in the first few hundred seconds and the rate of deposition decreases exponentially with time, in close agreement with the analytical solution. The results confirm that the bed level increases at the same rate as the water depth decreases and that the free surface elevation remains constant, thus conserving the mass of water and sediment.

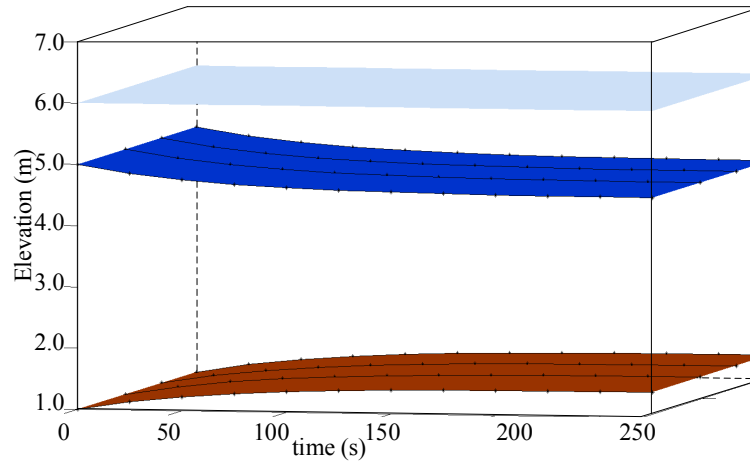


Figure 5. Evolution of deposition of suspended sediment in closed tank; bed elevation (brown), water depth (dark blue) and free surface elevation (light blue).

5.4. Entrainment in flat-bottomed tank of still water with no deposition

This test case is used to verify that the model can simulate the entrainment of sediment into suspension while conserving the mass of sediment and water. There is no deposition of suspended sediment. The numerical results are again compared to an analytical solution derived from Equations (48).

Following Soulsby [18], the entrainment flux E , is given by

$$E = \begin{cases} E_M \left(\frac{\tau_b - \tau_c}{\tau_c} \right) & \text{for } \tau_b > \tau_c \\ 0 & \text{otherwise,} \end{cases}$$

where τ_b is the total bed shear stress, τ_c is the critical bed shear stress and E_M is the entrainment constant. Here E is kept constant by fixing E_M , τ_b and τ_c as constants.

For constant entrainment of dilute suspended sediment in a frictionless, flat-bottomed tank with no net flow and no entrainment but intense vertical mixing, $u = 0$ and $D = 0$. As a result, Equations (48) solve to give

$$c(t) = 1 - \varepsilon - \frac{h_0(1 - \varepsilon)(1 - \varepsilon - c_0)}{(1 - \varepsilon)h_0 + Et}, \quad (52)$$

$$h(t) = h_0 + \frac{E}{(1 - \varepsilon)}t, \quad (53)$$

and

$$z_b(t) = z_{b0} - \frac{E}{(1 - \varepsilon)}t. \quad (54)$$

The initial free surface water elevation and bed elevation are again set to 6 m and 1 m above the datum, respectively. The bed shear stress, $\tau_b = 1 \text{ Nm}^{-2}$, the threshold bed shear stress, $\tau_c = 0.2 \text{ Nm}^{-2}$ and the entrainment constant, $E_M = 0.01 \text{ ms}^{-1}$. The numerical model is run until $t = 5000 \text{ s}$ with an initial concentration of suspended sediment equal to zero. The numerical predictions are in perfect agreement with the analytical solution. Figure 6 shows that the concentration of suspended sediment increases at a constant rate with time, as would be expected given that the entrainment is constant.

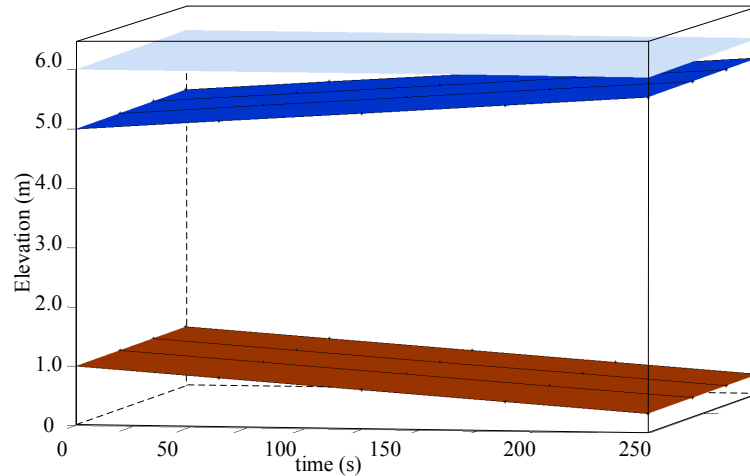


Figure 6. Evolution of entrainment of bed material into suspension in closed tank (bed elevation (brown), water depth (dark blue) and free surface elevation (light blue)).

The bed elevation decreases at the same rate as the depth of water increases. The excellent agreement between the model prediction and the analytical solution confirms that the mass of sediment and water is conserved.

5.5. Dam Break over a Bed Step

To demonstrate the need to use the well-balanced shallow water-sediment equations (40) under certain conditions, thus improving the general applicability of the numerical model, a test case of variable-density dam break flow over a bed step is presented, which includes a discontinuity in fluid density, similar to test cases presented by Murillo & Garcia-Navarro [10].

The dam, located at the centre of a 300 m long channel (at $x = 0$ m), is instantaneously removed at $t = 0$ s. Initially, the upstream and downstream water depths are 4 m and 0.78 m, respectively. For $x \leq 0$, $z_b = 0$ m and $c = 0.8$. For $x > 0$, $z_b = 1.5$ m and $c = 0.0$. The bed is fixed and $D = E = 0$.

This test case is run with three different numerical models. In the first instance, DB1, the water depth-discharge formulation of the governing equations (1) is used. It is clear from Figure 7(a) that this formulation of the equations is not well balanced and cannot account for the pressure change at the bed step. Equation (40) is used for the two other instances. No additional treatment of the density term is used at the bed step for DB2. As seen in Figure 7(b), when (40) is used, a discontinuity develops in the concentration profile at the bed step. This is due to the fact that c is a function of M , M_S and z_b . When there is a large discontinuity in z_b with respect to η , an unphysical discontinuity is produced in the concentration profile. In order to account for this, a simple upwinding treatment is used in DB3 to update c at the location of a vertical bed step. As seen in Figure 7(c), the upwinding eliminates the discontinuity.

Figure 7 (d) confirms Equation (31); the velocity is constant across the shear wave associated with the density discontinuity.

Although this test case shows that, in theory, the well-balanced governing equations are required to avoid unphysical discontinuities in the density profile at a bed step, it should be noted that the bathymetry is not discontinuous for most of the laboratory data presented in the literature for variable density flows. As such, further laboratory studies are necessary to validate numerical models for real engineering scenarios of water-sediment flow over sharp discontinuities.

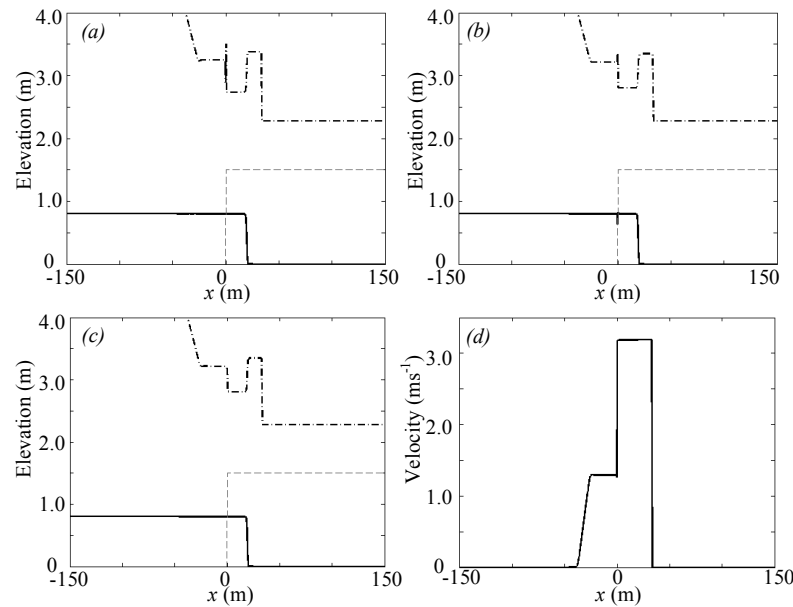


Figure 7. Variable density dam break over a bed step: spatial profiles at $t = 6$ s of concentration (solid line), free-surface elevation (dashed-dot) and bed elevation (dashed line) for (a) unbalanced equations (6) (b) well-balanced equations and (c) well-balanced equations including a simple upwinding treatment of $c(i)$ at the bedstep. The velocity profile at $t = 6$ s is given in (d).

6. VALIDATION AGAINST NUMERICAL AND LABORATORY EXPERIMENTS

6.1. Partial dyke breach in a rectangular laboratory-scale basin with non-erodible bed

Figure 8 presents the layout of an experiment carried out by Stelling and Duinmeijer [34] who investigated a dyke breach flood onto a flat, horizontal basin, 28.9 m long and 8 m wide in the Fluid Mechanics Laboratory of Delft University of Technology, the Netherlands. This test was also numerically modelled using finite volume schemes by Liang Q. *et al.* [35], Liang D. *et al.* [36], Cui *et al.* [37] and Li *et al.* [38]. The reservoir upstream of the dam wall initially contains still water of

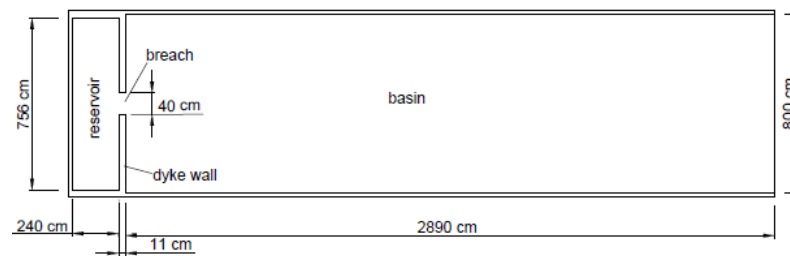


Figure 8. Delft University of Technology partial dyke breach: plan view set up of the laboratory basin.

depth 0.6 m. The section of the basin downstream of the wall is initially set to contain still water 0.05 m deep. At time, $t = 0$ s, a sluice gate, 40 cm wide, located in the centre of the dam is opened. For comparison purposes, Manning's roughness coefficient of $0.012 \text{ s m}^{-1/3}$ is chosen following Stelling and Duinmeijer [34]. The computational domain is discretised on a uniform mesh of square grid cells, each of length $\Delta x = \Delta y = 0.078$ m. The time step, $\Delta t = 0.01$ s is chosen to ensure stability. Slip boundary conditions are imposed at all of the walls, except at the outflow, an open, transmissive boundary. Figure 9 shows the results for the free surface elevation distributions and contours at $t = 4$ s and $t = 18$ s. Initially, the high-velocity jet emanating from the gate causes the water to

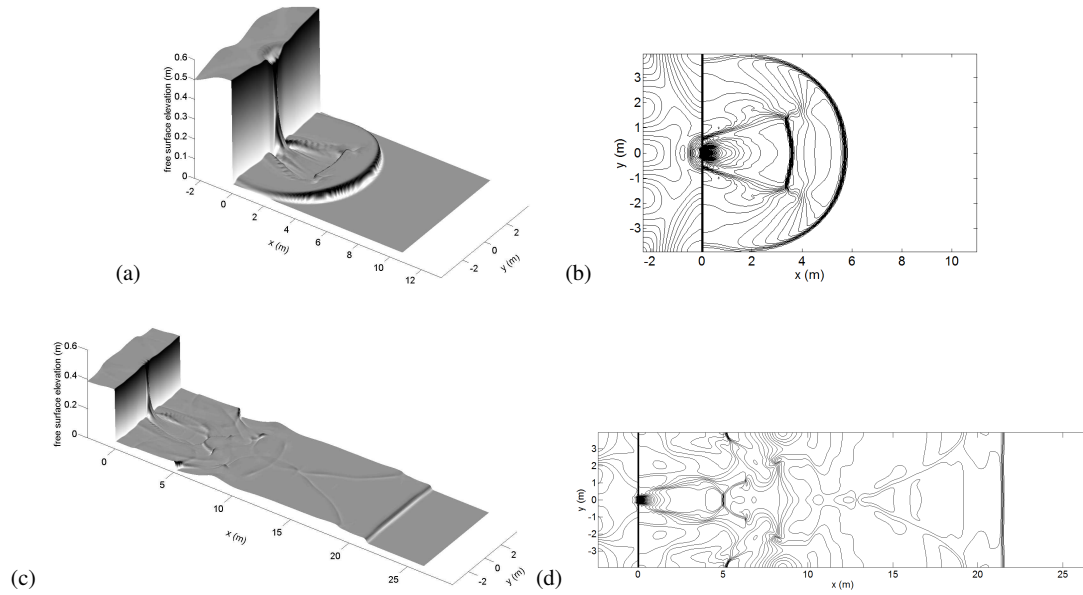


Figure 9. Delft University of Technology wet-bed partial dyke breach: surface and contour plots at $t = 4$ s and $t = 18$ s.

spread laterally as well as causing the bore to propagate downstream from the gate. This results in a symmetrical, almost semi-circular wave front propagating away from the gate. The bore is followed by a rarefaction wave which is pushed downstream by the high discharge from the gate, resulting in reflection and sloshing in the reservoir (see Figure 10a, Figure 9). At $t = 4$ s (Figure 9a), the primary bore wave has reached the sides of the channel and is reflected back into the channel. The reflected waves interact with a water plateau behind the bore front, resulting in the formation of an increasingly complicated wave pattern, symmetric about the centre of the channel. Interaction

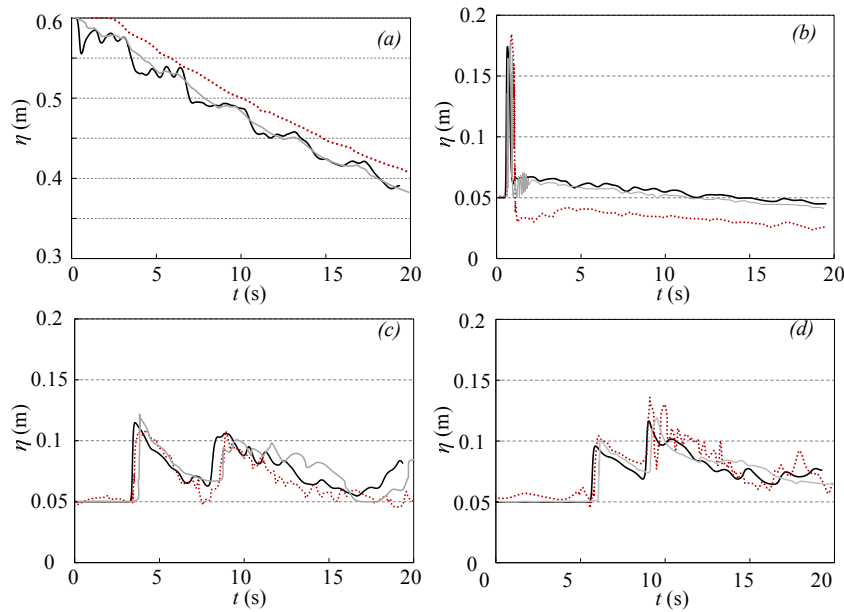


Figure 10. Delft University of Technology wet-bed partial dyke breach: time history plots at different gauge locations (-1 m, 1 m, 6 m, 13 m from gate) along the centre of the basin for laboratory data (red dotted line), numerical model of [34] (grey line) and present numerical model (solid black line).

between the reflected wave and the bore front results in the formation of a Mach stem, causing the primary bore front to become uniform across the basin by $t = 18$ s (Figure 9c). By $t = 18$ s (Figure 9c) the rarefaction wave behind the bore is held almost stationary about 5 m downstream of the gate by the supercritical flow issuing through the sluice. Meanwhile, the wave pattern becomes increasingly complicated with time due partly to side wall interactions. A full description of the flow physics is given by Liang Q. et al. [35].

The time history plots of the free surface elevation at different gauge points are in satisfactory agreement with the experimental results and in very good agreement with the numerical results of Liang et al. [35], validating that the numerical model is capable of properly simulating complicated flow hydraulics over a flat horizontal bed. In Figure 10 (a), more fluctuation is observed in the free surface elevation in the numerical model than in the experimental model. These exaggerated variations were also observed by [35] and could be a result of the difficulty in modelling the fast moving flow through the gate.

Allowing for the above discrepancies, the overall results obtained by the present numerical model are in close agreement with the numerical results obtained by Stelling and Duinmeijer [34] and Liang Q. et al. [35], shown in Figures 9 and 10. The limitations of the shallow-water equations also contribute to the differences between the observed experimental results and computed free surface elevation profiles, an example of the difficulties faced by numerical models which attempt to describe complicated shallow-water flows.

Although this test case does not consider sediment transport, the geometry of the experiment is similar to Test Case 6.3. The hydrodynamics presented above will be used to explain qualitatively the final bed topography of Case 6.3.

6.2. Idealised dam break over mobile bed

To test the capacity of the model to simulate accurately the interaction between a mobile bed and rapidly-varying dam break flow dynamics and to investigate further the eigenvalue problem of the variable-density governing equations, numerical solutions are compared to a numerical test presented by Cao *et al.* [1] of a 1D idealised dam break over a mobile bed. The dam, placed at the

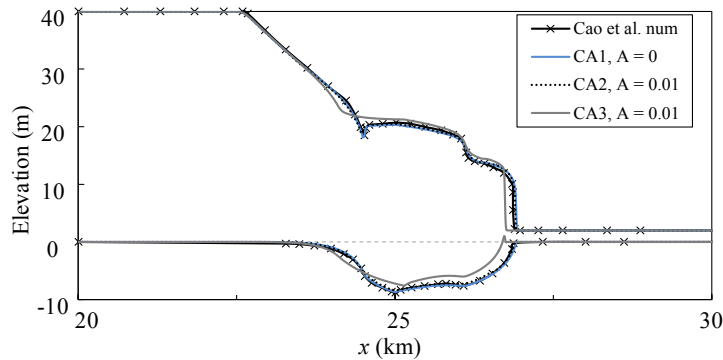


Figure 11. Cao *et al.* (2004) dam break: bed elevation and free surface elevation (m) 2 minutes after the dam is released. Numerical results (solid or dashed lines) plotted alongside numerical results of [1] (x). Initial bed level is also included (dashed line).

centre of a 50 km long channel, separates initial upstream and downstream river depths, 40 m and 2 m, respectively. The bed is composed of uniform sediment, $d = 4$ mm, and is erodible along the entire channel length. For simplicity, in place of equation (8), the bedload discharge components in the x and y directions are expressed using the Grass formula [39],

$$q_{bx} = Au(\sqrt{u^2 + v^2})^{m-1}, \quad (55a)$$

$$q_{by} = Av(\sqrt{u^2 + v^2})^{m-1}, \quad (55b)$$

where A is a dimensional constant, which incorporates the effects of grain diameter and kinematic viscosity, and m is a power parameter, normally chosen in the range $1 \leq m \leq 4$ (Hudson and Sweby [24]).

Three different variations of the test case were modelled; CA1, CA2 and CA3. In CA1, all of the

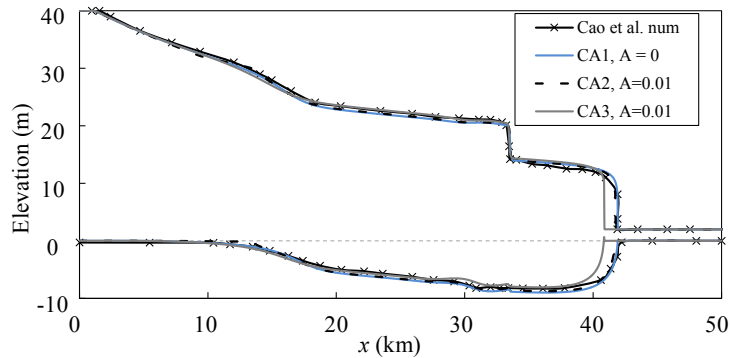


Figure 12. Cao *et al.* (2004) dam break: bed elevation and free surface elevation (m) 20 minutes after the dam is released. Numerical results (solid or dashed lines) plotted alongside numerical results of [1] (\times). Initial bed level is also included (dashed line).

parameters were chosen to be identical to those used by [1], including the grid size, $\Delta x = 10$ m and entrainment coefficient, $\alpha_e = 0.015$, and the Grass constant in equation (55), $A = 0 \text{ s}^2\text{m}^{-1}$, i.e. only suspended sediment is considered. In CA2 $A = 0.01 \text{ s}^2\text{m}^{-1}$ and the Rouse number condition (Section 2.2) is used to determine the dominant transport process. For CA3, $A = 0.01 \text{ s}^2\text{m}^{-1}$ but the Rouse number is not used, i.e. it is assumed that both bedload transport and suspended sediment transport occur simultaneously for all $t > 0$. The third case is similar to the model proposed by Benkhaldoun *et al.* [25].

Figures 11 and 12 show the results for bed elevation and free surface elevation at $t = 2$ min and $t = 20$ min, respectively. Figure 13 shows the volumetric concentration of suspended sediment

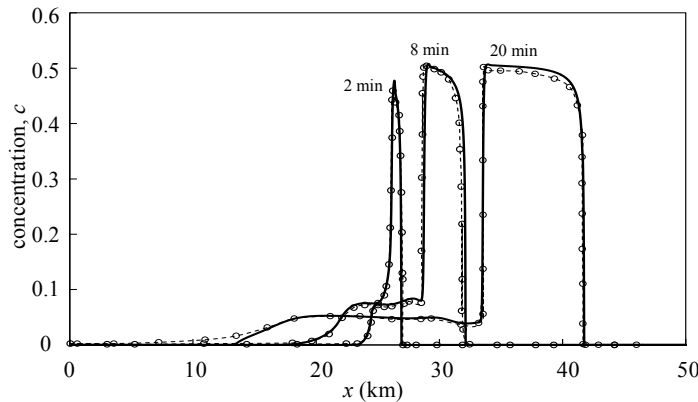


Figure 13. Cao *et al.* (2004) dam break: volumetric concentration of suspended sediment after 2 min, 8 min and 20 minutes. Numerical results (solid lines) are plotted against results obtained by [1] (dotted lines with circles).

as it evolves from $t = 2$ min to $t = 20$ min for case 1 only. In Figures 11 and 12, there is very little difference between the results of CB1 and CB2, and these are in perfect agreement with the numerical results computed by [1]. This confirms the assumption made by Cao *et al.* [1] that suspended sediment is the dominant transport mechanism. **Consideration of the Rouse number, presented in Figures 15 and 16, further validates that suspended sediment transport dominates. It is clearly evident in Figures 14(d), 15, and 16 that most of the bed erosion occurs under the fast**

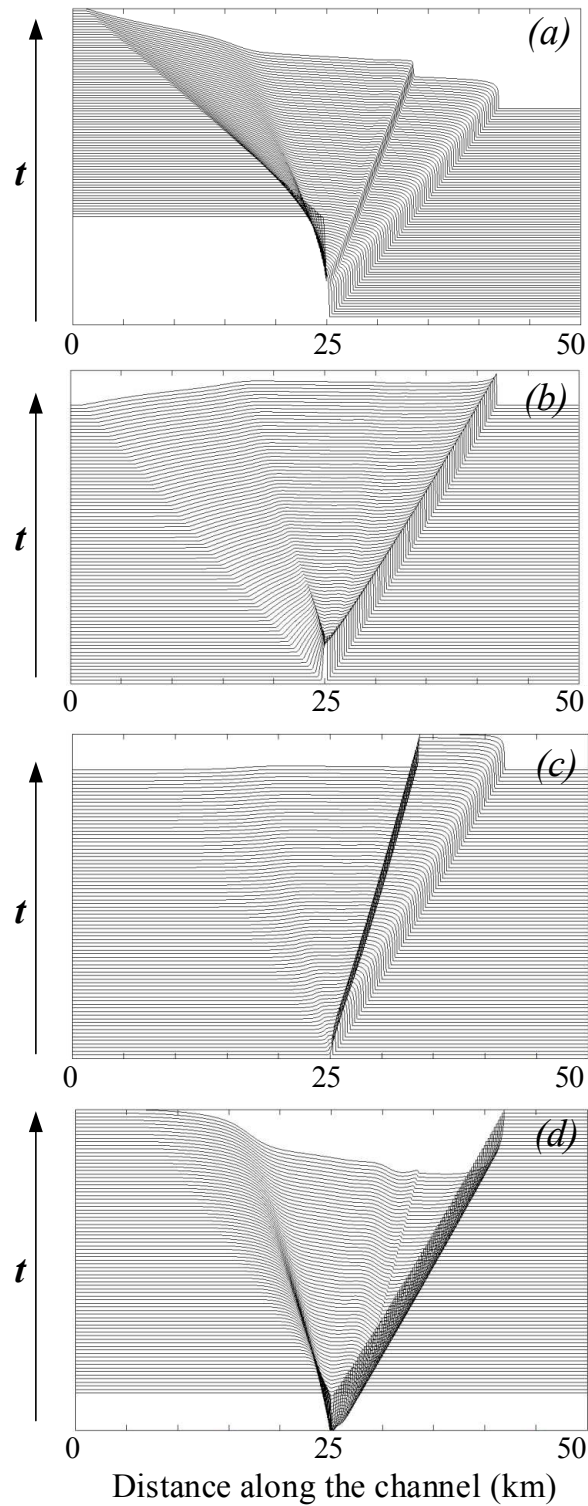


Figure 14. Cao *et al.* (2004) dam break: stacked $x - t$ plot for (a) the free surface elevation (m), (b) the streamwise velocity, u , (c) suspended sediment concentration and (d) bed elevation (m) for $t \leq 20$ minutes.

moving bore front. In Figure 15(a), $R_n \leq 1.3$ at the bore front for all $t > 0$, i.e. bed morphology is primarily a result of suspended sediment transport at this location. This is shown in greater detail for

$t = 0.25$ s and $t = 0.5$ s in Figure 16, where the instantaneous z_b profile is plotted with the profile of $R_n \leq 1.3$. Under the plateau following the bore front (Figure 15b,c), $1.3 < R_n \leq 2$, and little further erosion is observed in this region.

As expected following the above observations, in CB3, where bedload transport is assumed to occur for all $t > 0$ (CB3; R_n not considered; $A = 0.01$), the bed elevation and free surface elevation profiles are somewhat different from CB1 and CB2. The results of CB3 are very similar to the results obtained by [25] who made the same assumptions used in CB3, although [25] proposed a different method of solving the bed morphological equation (40e). These results highlight the importance of the Rouse number condition and the sensitivity of the final results to the sediment transport equations used in the model.

An important aspect of this test case to note is that the excellent agreement with [1], who used an HLLC solver of the water depth-discharge form of the shallow water-sediment equations, confirms the assumption made in Section 3.2; the same wave speed estimates can be used for the well-balanced form of the governing equations, even when the Jacobian matrices of the two systems are not identical.

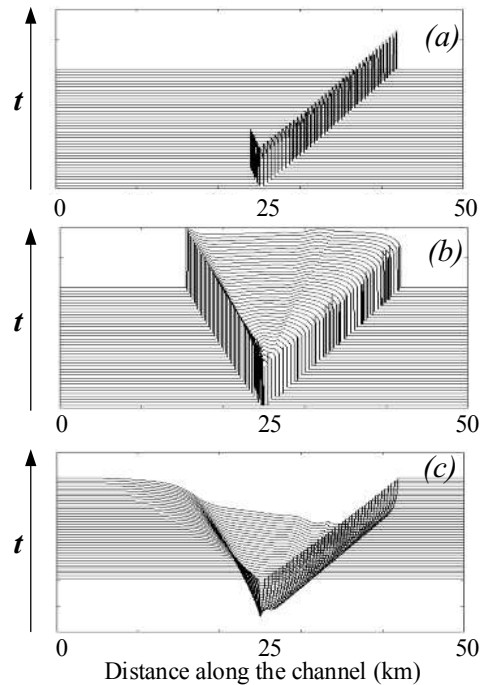


Figure 15. Cao *et al.* (2004) dam break: stacked $x - t$ plot for (a) $R_n \leq 1.3$, and (b) $1.3 < R_n \leq 2$ and (c) bed elevation z_b .

Figure 14 shows the stacked $x - t$ plots of the evolution of free surface elevation η , the horizontal flow velocity u , the volumetric concentration c and the bed elevation z_b from time $t > 0$ to $t = 20$ min. After the initial dam break, a large volume of sediment is entrained into suspension as the fast moving bore front passes along the bed. The fast-moving bore front continues to entrain sediment as it propagates downstream, creating a deep scour hole in the region between the bore front and the contact discontinuity. This contact discontinuity, which is represented by a sharp increase in free surface elevation and a sharp decrease in sediment concentration, marks the interface between the highly concentrated water-sediment mixture in the bore and the region of lower volumetric concentration of sediment. The sharp increase in free surface elevation at this point ensures that there is mass conservation of the water-sediment mixture, and that the hydrostatic pressure assumption made in the derivation of the governing equations is not violated. Upstream of the initial dam location ($x < 25$ km), a small amount of bed erosion is observed due to the passing of the rarefaction wave, but only in the region where the velocities are large enough for the bed shear

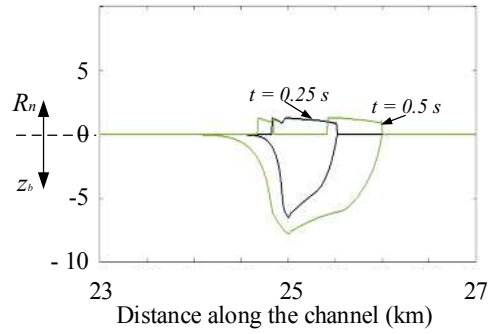


Figure 16. Cao *et al.* (2004) dam break: z_b and $R_n \leq 1.3$ profiles at $t = 0.25$ s (black) and $t = 0.5$ s (green).

stress to exceed the critical shear stress. Investigating the wave celerities and eigenvalues of the dam break problem, the local dynamic wave velocity, $a = \sqrt{gh}$, of the bore front is approximately 14 ms^{-1} . Figure 17 shows the waves, S_1 to S_4 , which demark the leading faces of the shock, rarefaction

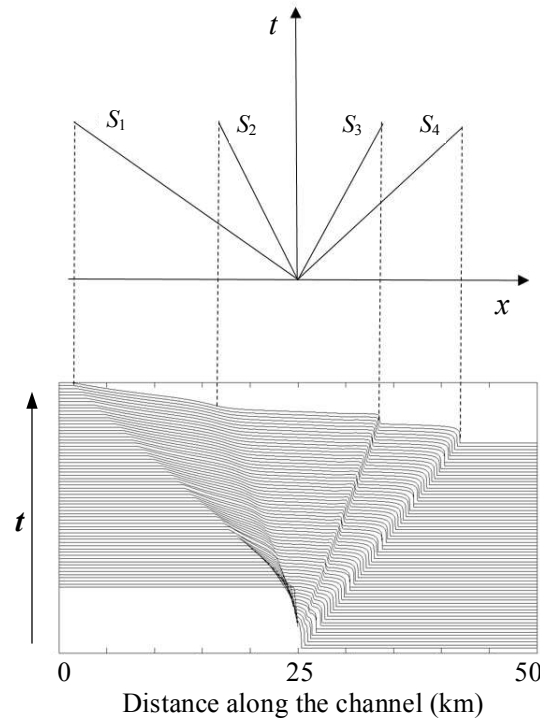


Figure 17. Cao *et al.* (2004) dam break: characteristic wave structure of the dam-break flow over mobile bed. (dotted lines with markers).

and shear waves. The speeds of these waves are calculated using the $x - t$ plot in Figure 14, where $S_1 = -19.3 \text{ ms}^{-1}$, $S_2 = -6.3 \text{ ms}^{-1}$, $S_3 = 7.05 \text{ ms}^{-1}$ and $S_4 = 14 \text{ ms}^{-1}$. S_1 is the left rarefaction wave speed, S_4 is the right shock wave and bore front wave speed, and $S_2 \approx S_3$ is the contact wave speed. These wave speeds are in agreement with the eigenvalue problem where,

$$\lambda_1 = u_1 - a = 0 - \sqrt{gh_1} = -\sqrt{(9.81)(40)} = -19.8 \text{ ms}^{-1} = S_1,$$

$$\lambda_2 = S_* = 7 \text{ ms}^{-1} = S_2 = S_3,$$

$$\lambda_3 = u_2 + a = 0 + \sqrt{gh_2} = \sqrt{(9.81)(20)} = 14 \text{ ms}^{-1} = S_4,$$

where u_1 and h_1 are the flow velocity and water depth upstream of the rarefaction wave, u_2 is the flow velocity downstream of the shock wave, h_2 is the water depth of the shock wave and S_* is the flow velocity of the plateau which develops between the rarefaction and shock waves. This provides further verification of the numerical solver, in that the eigenvalues (Equation (17)) are the same for the variable-density and constant density cases, except for an additional eigenvalue in the variable-density case which represents the contact discontinuity in fluid density.

6.3. Experimental 2D Dam Break over mobile bed

The final test case considers a 2D dam break experiment conducted in the Hydraulics Laboratory, Université Catholique de Louvain, within the framework of the NSF-Pire project (Soares-Frazão *et al.* [40]). The flume was 3.6 m wide and had a test length of 27 m. The mobile bed, initially 0.085 m deep, was spread 1 m upstream and 9 m downstream of the dam wall. In the rest of the flume, the horizontal, flat bed was fixed. The sediment had a median grain size $d = 1.61$ mm and relative density $s = 2.63$. The mobile bed porosity was $\varepsilon = 0.42$. The Manning coefficient was estimated as $n = 0.0165 \text{ s m}^{1/3}$ for the mobile bed and $n = 0.01 \text{ s m}^{1/3}$ for the fixed bed. The initial water level was 0.51 m upstream and 0.15 m downstream. A 1 m wide dam breach, induced by rapidly lifting a gate located at $x = 0$ m (Figure 18), created a laterally and longitudinally expanding wave. The experiment was run for 20 s, after which time the gate was closed and the flow stopped. At 8 gauge locations (see Figure 18 and Table I) the water level was measured every 0.1 s for the 20 s duration using ultrasonic gauges. The final bed elevation was then measured from $x = 0.5$ m to $x = 8$ m every 0.05 m (Figure 20).

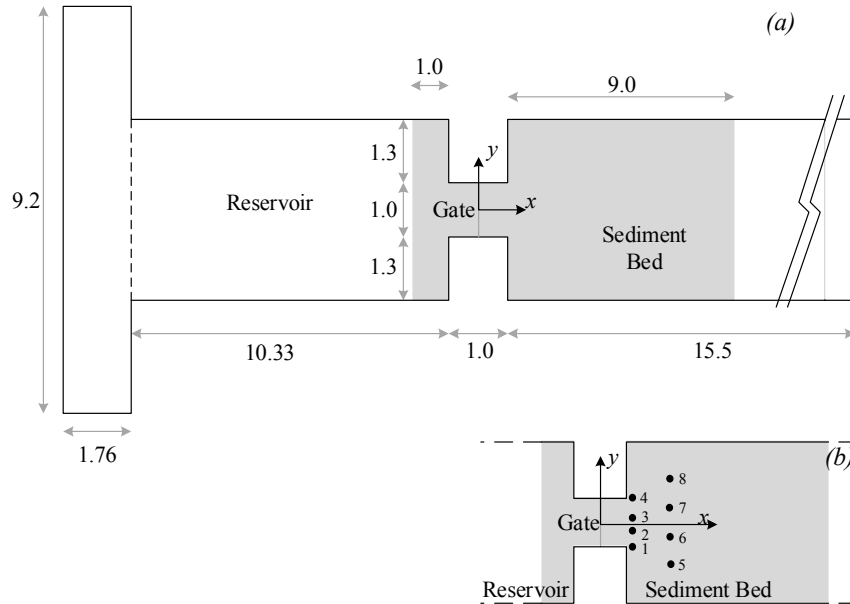


Figure 18. Plan view of (a) the experimental set up and (b) the location of the water depth gauges for the 2D partial dam break experiment at the Université Catholique de Louvain (UCL, Soares-Frazão *et al.* [40]).

The computational domain is discretised on a uniform mesh of square cells, each of length $\Delta x = \Delta y = 0.05$ m, with the time step Δt set to 0.01 s in order to ensure stability. Slip boundary conditions are imposed at all walls, with an open, transmissive boundary at the outflow. Two numerical tests were run using different closure relationships for the sediment transport, CB1 and CB2. **In this test case, $R_n \geq \approx 2.35$ for all $t > 0$ s.** Thus, bedload is the predominant mode of transport. In CB1, the entrainment and deposition coefficients E and D , are set to zero and Equation (40e) reduces to a traditional Exner-type bed morphology equation, where the bedload discharge is calculated using the Meyer-Peter-Mueller formula (8). For CB2, the bedload discharge components q_{bx} and q_{by} are neglected and E and D are used to model the sediment transport following the

approach of Cao *et al.* [41] such that

$$E = \alpha_d w_s c_{eq}, \quad D = \alpha_d w_s c. \quad (56)$$

When bedload transport is considered, the bedload transport capacity concentration c_{eq} , used to estimate the erosion rate associated with bedload, is given by

$$c_{eq} = \frac{hu}{q_b}. \quad (57)$$

In Equation (58) the unit-width bedload discharge is calculated at the centre of the grid cell using the Meyer-Peter-Mueller formula; $q_b = 8\sqrt{(s-1)gd^3}(\theta - \theta_c)^{3/2}$. If suspended sediment is also considered (i.e. where $R_n < 2.5$), the suspended sediment transport capacity concentration is used to estimate the erosion rate due to suspended sediment following Guo [42],

$$c_{eq} = \frac{1}{20} \frac{(u^3/ghw_s)^{1.5}}{1 + (u^3/ghw_s)^{1.15}}. \quad (58)$$

Although erosion due to suspended sediment is included in CB2 for completeness, it is noted that, for this test case, the results are very similar if suspended sediment is neglected because $R_n \geq 2.35$ for all $t > 0$. The empirical coefficient, α_d accounts for the difference between the depth-averaged concentration and the near-bed concentration. As suggested by [41], α_d is defined as the ratio of the flow depth to the thickness of the bedload layer,

$$\alpha_d = \frac{h}{\delta_b}, \quad (59)$$

in which $\delta_b = \min(2d, 9\theta d)$, such that the minimum bedload layer thickness is twice the particle diameter. Use of E and D , by definition, does not account for bedload transport in the traditional manner, since sediment is entrained into suspension. However, combining Equation (56) with the appropriate closure relationships, Equations (59) and (58), ensures that the depth-averaged concentration remains small; $c \leq 0.01$ in this case. Following from Equation (4), the density of the fluid is not significantly altered. As a result, when bedload transport dominates, the flow hydrodynamics are not affected significantly by the presence of suspended sediment and are impacted solely by changes in bed morphology, as would be expected for bedload transport mechanisms. These two cases are used to validate the accuracy of the numerical solver, to investigate the uncertainty which lies in the choice of closure relationships and to highlight the importance of using fully-coupled solvers to model accurately the interaction between highly unsteady flows and sediment transport.

Figure 19 compares the free surface elevation time histories for cases CB1 and CB2 with the measured results. Noting that the numerical model results are symmetric about $y = 0$ m, results at gauges 1, 2, 5 and 6 are shown in Figure 19. In both cases, there is satisfactory agreement between the numerical predictions and the experimental data; in particular the celerity and amplitude of the bore front are well captured at all gauges, although there are some discrepancies at US1, located at the corner of the dam wall. A similar finding was reported by Swartenbroekx *et al.* [43], who noted that the 2D depth-averaged model is unable to account for the turbulent shear stresses due to the vertical wall at the corner, which would act to slow down the flow as observed in the laboratory experiment results. Both CB1 and CB2 yield almost identical results at $t < 5$ s, validating the assumptions outlined above in using Equation (56). After this time, the scour hole has evolved differently for the two cases, and this affects the free surface elevation. For $t > 5$ s, at US6 the predicted free surface varies less than the measured free surface. From the contour plot of the final bed topography (Figure 20) it can be seen that a second scour hole has formed at US6 in the experiment which is not reproduced by either of the numerical models. The large variation in η observed at US6 in Figure 19 can be attributed to the presence of this scour hole.

A prominent feature of the experimental results is the well-defined undulations in the final bed topography, seen in Figure 20(a). In the literature, the absence of bedforms in shallow water

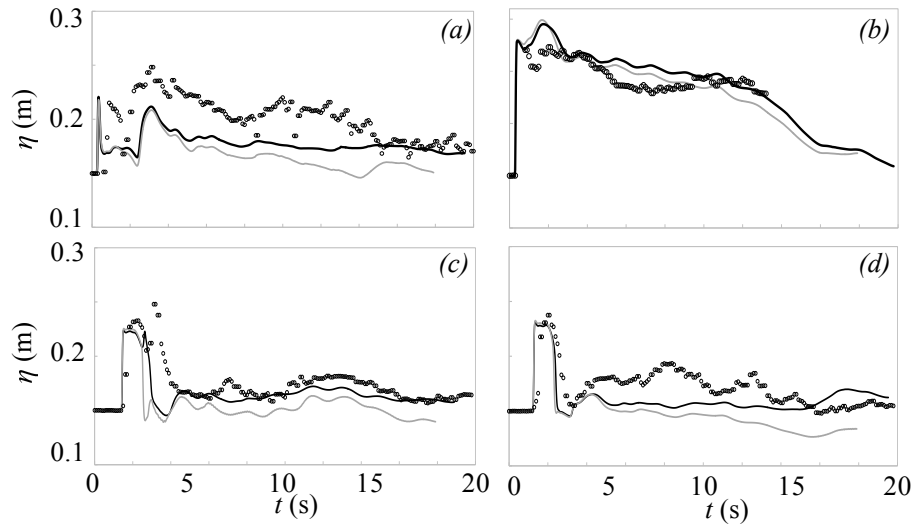


Figure 19. Université Catholique de Louvain partial dam breach: free surface elevation profiles for the experimental results (circles), CB1 (grey solid line) and CB2 (black solid line) at gauge location (a) US1, (b) US2, (c) US5 and (d) US6.

simulations of dam break flows concerning bedload transport is often attributed to the limitations of the depth-averaged equations which cannot account for vertical accelerations (e.g. [3], [44], [45]). Indeed, the vertical accelerations do impact scour and resulting bedforms, particularly immediately downstream of a dam break, where the vertical component is a defined feature of the flow (see for example [3]). It would be reasonable to conclude that the underestimation of the first scour hole when comparing measurements and numerical results, as seen in Figures 20 and 21 is primarily due to the absence of this vertical velocity component in the shallow-water model. There are, however, other physical mechanisms which could be responsible for the undulations seen further downstream, at $x > 2.5$ m. Notably, these bedforms appear to have very similar features to cyclic steps, formed during supercritical flow over an erodible bed (e.g. [46]). Cyclic steps are widely observed in open channel flows [47]. They are particular bedforms bounded by hydraulic jumps which develop because erosion dominates under fast supercritical flow and deposition occurs at the point of transition from supercritical to subcritical flow. Although no measurements were available for the bed morphology during the course of the experiment, the process of erosion and deposition which produces cyclic steps, well-described by [46], is clearly visible in the numerical time history spatial profiles for CB2 in Figure 22. A well-defined hydraulic jump propagates downstream at the location where the rarefaction wave, associated with the primary bore front, meets the high-velocity flow emanating from the dam breach. Similar hydrodynamics were previously described in the discussion of Test Case 6.1, Figure 9. Sediment entrained by the fast supercritical jet emerging from the dam, seen in the deepening of the scour hole at $x < 3$ m over time, is deposited immediately downstream of this hydraulic jump, forming a hump in the bed profile. Because the hydraulic jump is pushed downstream by the high-velocity jet, the process of deposition is repeated downstream, forming a series of bed-humps. In Figure 22 it can be seen that the bedforms induce waves in the free surface, which sustain the bedforms allowing them to increase in size with time. Previously, cyclic steps have been reproduced successfully by several researchers, using 1D shallow-water models coupled with the appropriate relations for D and E (e.g. [48], [49]). To the author's knowledge, this process has not been well documented for more complex 2D shallow-water flows but merits future investigation.

Although in CB2, use of the formulation proposed by Cao *et al.* [41] does predict satisfactorily the undulated bed profile along the centre of the channel (see Figure 21a), from Figure 20, it is clear that the bedforms in the numerical model do not have the same planar shape as those observed in the laboratory. Rather, the final bed topography in CB2 follows a diagonal pattern (Figure 20c),

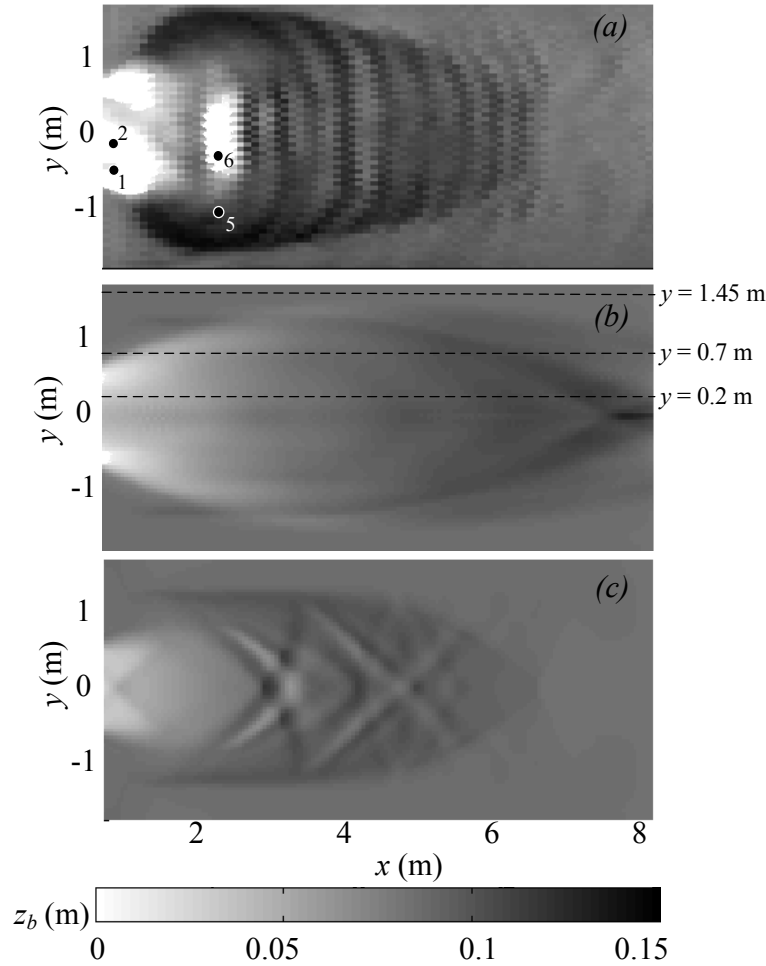


Figure 20. Université Catholique de Louvain partial dam breach: final bed topography contours for (a) measured data, (b) CB1 and (c) CB2. Black dots in (a) indicate locations of the water gauges, US1, US2, US5 and US6. Dashed lines in (b) indicate the locations of the bed profiles shown in Figure 21.

mirroring the complex free surface behaviour caused by the interactions of the bore with the flume walls, as seen in more detail in Test Case 6.1 (Figure 9). It is likely that additional momentum would have been removed from the flow to create the deeper scour hole formed at $x \approx 1$ m in the physical experiment. As a result, the intensity of the reflections of the bore front and side walls would have been reduced, which could have resulted in a more unidirectional flow, allowing for the hydraulic jump to spread across the entire channel width, as opposed to taking up the diagonal form seen in the numerical model. Because sediment deposition is directly related to the free surface pattern, and the resulting bed morphology strongly impacts the hydrodynamics, seen in Figure 22, a small difference in the initial free surface pattern could significantly affect the final bed topography.

Soares-Frazão *et al.* [40] note that bed undulations were not captured by most of the shallow water models in the initial NSF-Pire project, although certain models which used a very fine mesh ($\Delta x = 0.02$ m) did reproduce qualitatively some bedforms. Interestingly, the latter models used either two-layer depth-averaged schemes with closure relationships for sediment transport based on the local bed shear stresses (e.g. [43]), or else the formulation used in CB2, which allows for local entrainment and deposition of particles [41]. This is an important finding, reiterated in the present study, which encourages further research into refining the sediment transport model used in CB2 and other such models which allow for local entrainment and deposition, even when bedload transport appears to be the dominant process (for example when $R_n \approx 2.5$).

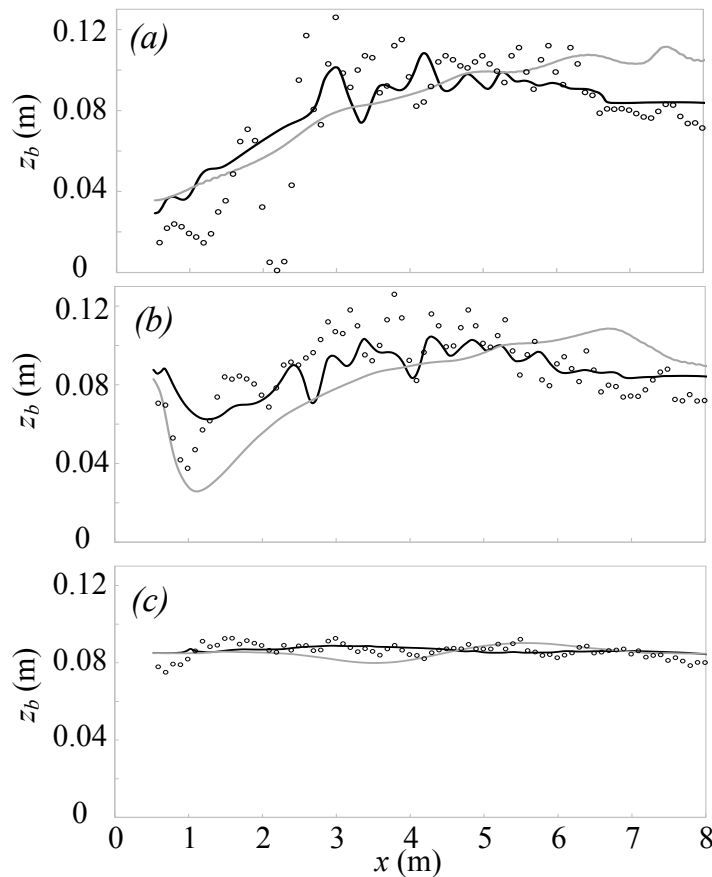


Figure 21. Université Catholique de Louvain partial dam breach: final bed profiles from $x = 0.5$ m - 8.0 m; (a) $y = 0.2$ m, (b) $y = 0.7$ m, (c) $y = 1.45$ m; for measured data (circles), CB1 (grey solid lines) and CB2 (black solid lines).

In the absence of more detailed experimental measurements of the free surface elevation along the entire length of the erodible bed, as well as measurements of bed morphodynamics during the course of the experiments, the latter which are difficult to obtain in practice, the above explanation is not intended as an absolute description of the physical processes which occurred during the experiment. It is presented as an interesting qualitative analysis of highly coupled water-sediment interactions and offers an alternative interpretation of the formation of bedforms under dam break flows.

One of the main conclusions of Soares-Frazão *et al.* [40], through comparison of various numerical model results with the measured data, is that a major uncertainty in sediment transport modelling lies in the choice of empirical formulae and closure relationships. This is reiterated in the present work, where the final bed topography profiles vary significantly depending on the closure model used, even though all other aspects of the numerical solver are identical in both cases. In addition, the present results suggest that oscillations observed in dam break flows over mobile, granular beds cannot be attributed solely to vertical accelerations, as often suggested in the literature ([3], [44]). Indeed, it appears that even when bedload transport dominates under certain conditions, local erosion and deposition of particles may be responsible for the final bed morphology. In light of this, future numerical studies of bedload transport caused by dam break flows, which consider alternative approaches to the Exner-type equation and admit local entrainment and deposition of particles, merit investigation.

This validation case highlights another advantages of this numerical model; it can be used to investigate a very wide range of sediment transport formulae, from the Exner-type equations for bedload transport to the total load transport form of the sediment transport equations. Thus, it could

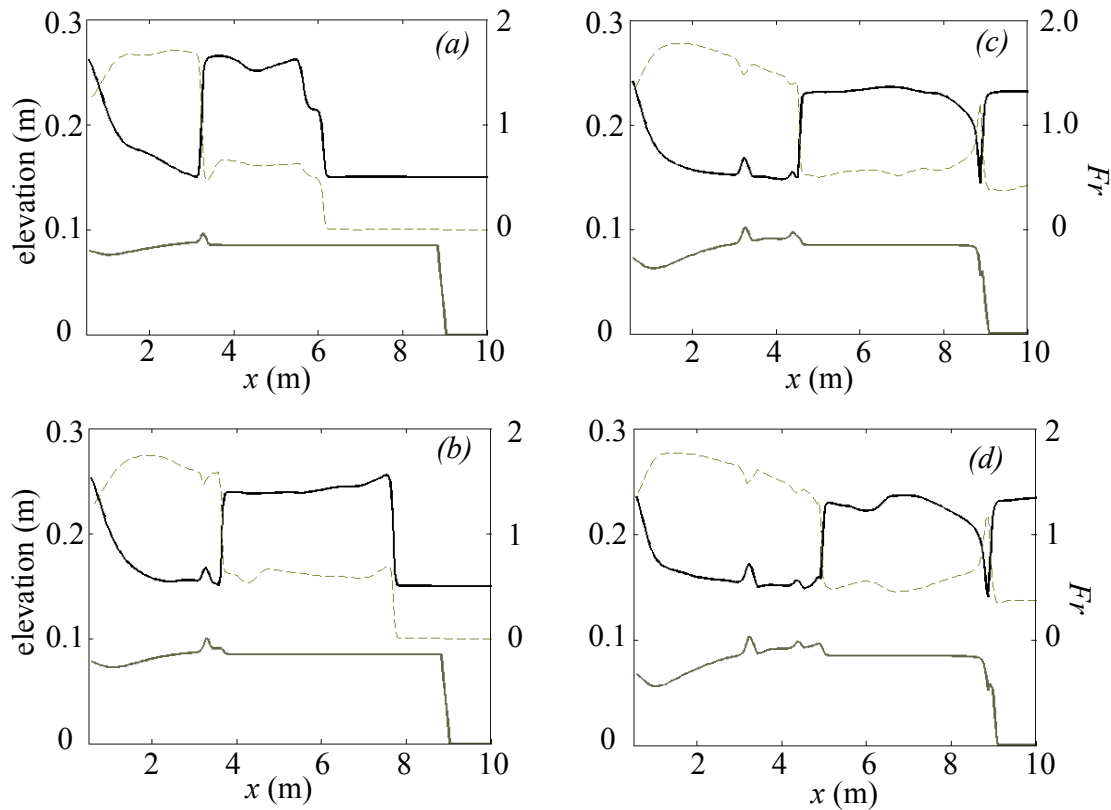


Figure 22. Université Catholique de Louvain partial dam breach: spatial profiles of free surface elevation (solid black line), bed elevation (solid grey line) and Froude no. (dashed line) at (a) $t = 4$ s, (b) $t = 5$ s, (c) $t = 8$ s and (d) $t = 10$ s.

be used for a large variety of engineering applications and different flow-sediment regimes, provided that care is taken when choosing the appropriate closure relationships.

7. CONCLUSION

A Godunov-type finite volume numerical scheme has been developed to solve the variable-density shallow water-sediment equations in their fully conservative, coupled form for flow dynamics, sediment transport and bed morphological change. The solution of the Riemann problem for the conventional shallow-water equations has been extended to account for the variable-density property. The new equation derived to estimate this intermediate wave speed is a generalised form of the Toro [16] solution and includes the variable mass of the water-sediment mixture.

The well-balanced property of the final system of equations has been demonstrated, verifying that the equations are valid even in the presence of bed discontinuities. In order to facilitate the numerical scheme and solve directly for the variable-density conservation laws, dependent variables were specially selected in the mathematical formulation (as an alternative to the manipulation used by [1]).

Semi-analytical solutions were derived for suspended sediment entrainment and deposition in a flat-bottomed tank, with zero horizontal velocity. They were used to validate the present numerical model and could prove useful for benchmarking future suspended sediment transport models.

The numerical model has been validated successfully for both conventional bedload transport and suspended sediment transport. One major advantage of the present model is that it is valid for a wide range of bedload and suspended sediment transport formulae. Parameters can be chosen easily

to isolate one dominant mode of transport or consider a combination of both, extending the range of applicability of the model. The model is capable of simulating 2D rapidly varying flows and dam break-mobile bed interactions for uniform sediment particles. The present scheme reproduces exactly the numerical results of idealised dam-break flow over an erodible bed comprised of uniform sediment particles presented by [1], provided the correct type of sediment transport process is chosen, achieved using the Rouse number condition. The numerical predictions are in acceptable agreement with experimental results of a 2D dam break over a mobile bed both in capturing the flow hydrodynamics and the bed morphological changes. By comparing different methods for updating the bed morphological change, the limitations of the traditional Exner-type equation for bedload transport under fast, transient flows have been highlighted and this merits future investigation. The results presented in this paper validate that the shallow water-sediment equations can be solved in their unmanipulated form, reducing the complexity of the source terms when compared to the formulation presented by [1].

Further studies are required to validate the model against dam break scenarios involving complex two-dimensional flows over mobile beds composed of fine sediment, where the dominant mode of transport is in suspension. To extend the general applicability of the model, a wetting-and-drying algorithm should be included. Studies should also be carried out for cases where the bed is composed of non-uniform sediment particles, particularly for a large variety of particle sizes where heavier particles are transported as bedload and finer particles are transported in suspension.

A. DERIVATION OF PROPERTIES OF HLLC SOLVER FOR VARIABLE-DENSITY CASE

A.1. Rarefaction wave

Equating the first and fourth terms of Equation (20) we find

$$\frac{d\rho}{\rho} = \frac{dc}{c} . \quad (60)$$

This clearly implies that $\rho = \text{constant}$ and $c = \text{constant}$, considering the relationship between ρ and c , defined in Equation (5).

Using (60), the first two equations of (20) reduce to the constant density problem such that

$$v = \text{constant}, \quad \text{and} \quad u - 2a = \text{constant}.$$

Similar analysis of across the right rarefaction results in Equation (22).

A.2. Left Shock Wave

Across a left shock wave the Rankine-Hugoniot condition is written

$$\mathbf{f}(\mathbf{q}_{*L}) - \mathbf{f}(\mathbf{q}_L) = S_L(\mathbf{q}_{*L} - \mathbf{q}_L) , \quad (61)$$

where S_L is the speed of the left wave (see Figure 2). The conserved variables to the left of the star (or middle) wave q_{*L} , and to the left of the shock wave (which is the right of S_*) q_L are

$$\mathbf{q}_{*L} = \begin{Bmatrix} \rho_{*L} h_{*L} \\ \rho_{*L} u_{*L} h_{*L} \\ \rho_{*L} v_{*L} h_{*L} \\ \rho_s c_{*L} h_{*L} \end{Bmatrix} \quad \text{and} \quad \mathbf{q}_L = \begin{Bmatrix} \rho_L h_L \\ \rho_L u_L h_L \\ \rho_L v_L h_L \\ \rho_s c_L h_L \end{Bmatrix}$$

and the corresponding flux matrices are

$$\mathbf{f}(\mathbf{q}_{*L}) = \begin{bmatrix} \rho_{*L} u_{*L} h_{*L} \\ \rho_{*L} u_{*L}^2 h_{*L} + \frac{1}{2} \rho_{*L} g h_{*L}^2 \\ \rho_{*L} u_{*L} v_{*L} h_{*L} \\ \rho_s c_{*L} u_{*L} h_{*L} \end{bmatrix} \quad \text{and} \quad \mathbf{f}(\mathbf{q}_L) = \begin{bmatrix} \rho_L u_L h_L \\ \rho_L u_L^2 h_L + \frac{1}{2} \rho_L g h_L^2 \\ \rho_L u_L v_L h_L \\ \rho_s c_L u_L h_L \end{bmatrix} .$$

The Rankine-Hugoniot conditions for the first two equations of (61) are

$$\rho_{*L} u_{*L} h_{*L} - \rho_L u_L h_L = S_L (\rho_{*L} h_{*L} - \rho_L h_L) \quad (62)$$

and

$$\rho_{*L} u_{*L}^2 h_{*L} + \frac{1}{2} \rho_{*L} g h_{*L}^2 - (\rho_L u_L^2 h_L + \frac{1}{2} \rho_L g h_L^2) = S_L (\rho_{*L} u_{*L} h_{*L} - \rho_L u_L h_L) . \quad (63)$$

Transforming the frame of reference of the problem described by (61) to that moving with the speed of the shock wave, S_L , the relative velocities, \hat{u} , are:

$$\hat{u}_L = u_L - S_L, \quad \text{and} \quad \hat{u}_{*L} = u_{*L} - S_L. \quad (64)$$

Substituting (64) into (62) and (63), the RH conditions can be written in the transformed frame of reference as,

$$\rho_{*L} \hat{u}_{*L} h_{*L} = \rho_L \hat{u}_L h_L \quad (65)$$

and

$$\rho_{*L} \hat{u}_{*L}^2 h_{*L} + \frac{1}{2} \rho_{*L} g h_{*L}^2 = \rho_L \hat{u}_L^2 h_L + \frac{1}{2} \rho_L g h_L^2 . \quad (66)$$

Similarly, substitution of (64) into the third and fourth equations of (61) yields,

$$\rho_{*L} \hat{u}_{*L} \hat{v}_{*L} h_{*L} = \rho_L \hat{v}_L \hat{u}_L h_L \quad (67)$$

and

$$c_{*L} \hat{u}_{*L} h_{*L} = c_L \hat{u}_L h_L . \quad (68)$$

Rewriting (65) and substituting it into (68) we can write

$$\frac{\rho_L}{c_L} = \frac{\rho_{*L}}{c_{*L}} . \quad (69)$$

Combining (5) and (69), dividing both sides by $(\rho_s - \rho_w)$ and rearranging, we obtain

$$\rho_L = \rho_{*L} . \quad (70)$$

Dividing (67) by (62) confirms that $v_{*L} = v_L$, i.e. both the tangential velocity and the mixture density are constant across the shock wave.

Similar analysis can be performed across a right shock wave to yield the same results; $v_{*R} = v_R$ and $\rho_R = \rho_{*R}$.

A.3. Shear Wave - Density Discontinuity

Across the shear wave associated with a density discontinuity, using $\mathbf{R}^{(4)}$ the Riemann invariants give

$$\frac{\rho_s(\rho_w + \rho)d\rho h}{\rho(\rho_s - \rho_w)} = \frac{\rho_s(\rho_w + \rho)d\rho u h}{u\rho(\rho_s - \rho_w)} = \frac{d\rho v h}{0} = \frac{d\rho_s h}{1} . \quad (71)$$

Equating the first two terms and dividing by $\frac{\rho_s(\rho_w + \rho)}{\rho(\rho_s - \rho_w)}$, it is easily shown that $u = \text{constant}$. Similarly, $v = \text{constant}$ from the third term of (71). Now equating the first and last terms and substituting $c = \frac{\rho - \rho_w}{\rho_s - \rho_w}$, after some simple manipulation we can write,

$$2\rho dh + h d\rho = 0, \quad (72)$$

or, multiplying both sides by h and integrating, $\rho h^2 = \text{constant}$, validating the hydrostatic pressure assumption made in the initial derivation of the shallow water-sediment equations. Note here that if the bathymetry is variable, the change in bed elevation needs to be incorporated in the pressure term such that $\rho(h^2 - z_b^2) = \text{constant}$.

ACKNOWLEDGEMENTS

The authors would like to acknowledge Professor Richard Soulsby and Dr Kuo Yan for their various contributions to the analysis underpinning the mathematical model. The first-author would like to acknowledge IRCSET and The University of Edinburgh, through which her studies have been funded. The authors would also like to thank the anonymous reviewers for their comments which lead to a significantly improved final version of this paper.

References

1. Cao Z, Pender G, Wallis S, Carling P. Computational dam-break hydraulics over erodible sediment bed. *Journal of Hydraulic Engineering* 2004; **130**(7):689–703.
2. Cao Z, Carling P. Mathematical modelling of alluvial rivers: reality and myth. Part 1: General review. *Proceedings of the ICE-Water and Maritime Engineering* 2002; **154**(3):207–219.
3. Capart H, Young D. Formation of a jump by the dam-break wave over a granular bed. *Journal of Fluid Mechanics* 1998; **372**:165–187.
4. Castro Díaz M, Fernández-Nieto E, Ferreiro A. Sediment transport models in shallow water equations and numerical approach by high order finite volume methods. *Computers & Fluids* 2008; **37**(3):299–316.
5. Leighton FZ, Borthwick AG, Taylor PH. 1-d numerical modelling of shallow flows with variable horizontal density. *International Journal for Numerical Methods in Fluids* 2010; **62**(11):1209–1231.
6. Juez C, Murillo J, García-Navarro P. One-dimensional riemann solver involving variable horizontal density to compute unsteady sediment transport. *Journal of Hydraulic Engineering* 2015; **142**(3):04015 056, doi: 10.1061/(ASCE)HY.1943-7900.0001082.
7. Zhou JG. Lattice boltzmann morphodynamic model. *Journal of Computational Physics* 2014; **270**:255–264.
8. Simpson G, Castellort S. Coupled model of surface water flow, sediment transport and morphological evolution. *Computers & Geosciences* 2006; **32**(10):1600–1614.
9. Cao Z, Li Z, Pender G, Hu P. Non-capacity or capacity model for fluvial sediment transport. *Proceedings of the ICE-Water Management* 2012; **165**(4):193–211.
10. Murillo J, Latorre B, García-Navarro P. A riemann solver for unsteady computation of 2d shallow flows with variable density. *Journal of Computational Physics* 2012; **231**(14):4775–4807.
11. Murillo J, García-Navarro P. An exner-based coupled model for two-dimensional transient flow over erodible bed. *Journal of Computational Physics* 2010; **229**(23):8704–8732.
12. Juez C, Murillo J, García-Navarro P. A 2D weakly-coupled and efficient numerical model for transient shallow flow and movable bed. *Advances in Water Resources* 2014; **71**:93–109.
13. Apostolidou I. Variable density shallow flow model for flood simulation. PhD Thesis, University of Oxford 2011.
14. Jiang L, Borthwick AG, Krámer T, Józsa J. Variable density bore interaction with block obstacles. *International Journal of Computational Fluid Dynamics* 2011; **25**(4):223–237.
15. Toro EF, Spruce M, Speares W. Restoration of the contact surface in the harten-lax-van leer riemann solver. *Shock Waves* 1994; **4**:25–34.
16. Toro EF. *Shock-capturing methods for free-surface shallow flows*. Wiley, 2001.
17. Yan K. Coastal flood inundation and morphodynamic change. PhD Thesis, University of Oxford 2010.
18. Soulsby R. *Dynamics of marine sands: a manual for practical applications*. Thomas Telford, 1997.
19. Meyer-Peter E, Müller R. Formulas for bed-load transport. IAHR, 1948.
20. Cao Z. Equilibrium near-bed concentration of suspended sediment. *Journal of Hydraulic Engineering* 1999; **125**(12):1270–1278.
21. Zhang R, Xie J. *Sedimentation research in China: Systematic selections*. China and Power Press, 1993.
22. Fraccarollo L, Toro EF. Experimental and numerical assessment of the shallow water model for two-dimensional dam-break type problems. *Journal of Hydraulic Research* 1995; **33**(6):843–864.
23. Harten A, Lax PD, van Leer B. On upstream differencing and godunov-type schemes for hyperbolic conservation laws. *SIAM review* 1983; **25**(1):35–61.
24. Hudson J, Sweby PK. Formulations for numerically approximating hyperbolic systems governing sediment transport. *Journal of Scientific Computing* 2003; **19**(1-3):225–252.
25. Benkhaldoun F, Elmahi I, Sari S, Seaid M. An unstructured finite-volume method for coupled models of suspended sediment and bed load transport in shallow-water flows. *International Journal for Numerical Methods in Fluids* 2013; **72**(9):967–993.
26. Rogers BD, Borthwick AG, Taylor PH. Mathematical balancing of flux gradient and source terms prior to using Roe's approximate riemann solver. *Journal of Computational Physics* 2003; **192**(2):422–451.
27. Bermúdez A, Vázquez ME. Upwind methods for hyperbolic conservation laws with source terms. *Computers & Fluids* 1994; **23**(8):1049–1071.

28. Zhou JG, Causon DM, Ingram DM, Mingham CG. Numerical solutions of the shallow water equations with discontinuous bed topography. *International Journal for Numerical Methods in Fluids* 2002; **38**(8):769–788.
29. Benkhaldoun F, Elmahi I, Seaid M, *et al.*. Well-balanced finite volume schemes for pollutant transport by shallow water equations on unstructured meshes. *Journal of Computational Physics* 2007; **226**(1):180–203.
30. Murillo J, García-Navarro P. Energy balance numerical schemes for shallow water equations with discontinuous topography. *Journal of Computational Physics* 2013; **236**:119–142.
31. Liang Q, Borthwick AGL. Adaptive quadtree simulation of shallow flows with wet-dry fronts over complex topography. *Computers and Fluids* 2009; **38**(2):221–234.
32. Huang J, Borthwick AG, Soulsby RL. One-dimensional modelling of fluvial bed morphodynamics. *Journal of Hydraulic Research* 2008; **46**(5):636–647.
33. De Vries M. River-bed variations - aggradation and degradation. *I.H.A.R. International Seminar on Hydraulics of Alluvial Streams, New Dehli*, 1973; **Publication no. 107, 20 p.**
34. Stelling G, Duinmeijer S. A staggered conservative scheme for every froude number in rapidly varied shallow water flows. *International Journal for Numerical Methods in Fluids* 2003; **43**(12):1329–1354.
35. Liang Q, Borthwick A, Stelling G. Simulation of dam-and dyke-break hydrodynamics on dynamically adaptive quadtree grids. *International Journal for Numerical Methods in Fluids* 2004; **46**(2):127–162.
36. Liang D, Falconer RA, Lin B. Comparison between tvd-maccormack and adi-type solvers of the shallow water equations. *Advances in Water Resources* 2006; **29**(12):1833–1845.
37. Cui H, Pietrzak J, Stelling G. A finite volume analogue of the finite element: With accurate flooding and drying. *Ocean Modelling* 2010; **35**(1):16–30.
38. Li W, de Vriend HJ, Wang Z, Maren D. Morphological modeling using a fully coupled, total variation diminishing upwind-biased centered scheme. *Water Resources Research* 2013; **49**(6):3547–3565.
39. Grass A. *Sediment transport by waves and currents*. University College, London, Dept. of Civil Engineering, 1981.
40. Soares-Frazão S, Canelas R, Cao Z, Cea L, Chaudhry HM, Die Moran A, El Kadi K, Ferreira R, Cadórniga IF, Gonzalez-Ramirez N, *et al.*. Dam-break flows over mobile beds: experiments and benchmark tests for numerical models. *Journal of Hydraulic Research* 2012; **50**(4):364–375.
41. Cao Z, Hu P, Pender G. Reconciled bedload sediment transport rates in ephemeral and perennial rivers. *Earth Surface Processes and Landforms* 2010; **35**(14):1655–1665.
42. Guo J. Logarithmic matching and its applications in computational hydraulics and sediment transport. *Journal of Hydraulic research* 2002; **40**(5):555–565.
43. Swartenbroekx C, Zech Y, Soares-Frazão S. Two-dimensional two-layer shallow water model for dam break flows with significant bed load transport. *International Journal for Numerical Methods in Fluids* 2013; **73**(5):477–508.
44. Spinewine B, Capart H. Intense bed-load due to a sudden dam-break. *Journal of Fluid Mechanics* 9 2013; **731**:579–614.
45. Canelas R, Murillo J, Ferreira RM. Two-dimensional depth-averaged modelling of dam-break flows over mobile beds. *Journal of Hydraulic Research* 2013; **51**(4):392–407.
46. Kostic S, Sequeiros O, Spinewine B, Parker G. Cyclic steps: A phenomenon of supercritical shallow flow from the high mountains to the bottom of the ocean. *Journal of Hydro-environment Research* 2010; **3**(4):167–172.
47. Parker G, Izumi N. Purely erosional cyclic and solitary steps created by flow over a cohesive bed. *Journal of Fluid Mechanics* 2000; **419**:203–238.
48. Sun T, Parker G. Transportational cyclic steps created by flow over an erodible bed. part 2. theory and numerical simulation. *Journal of Hydraulic Research* 2005; **43**(5):502–514.
49. Balmforth N, Vakil A. Cyclic steps and roll waves in shallow water flow over an erodible bed. *Journal of Fluid Mechanics* 2012; **695**:35–62.

Gauge	x (m)	y (m)
US1	0.640	-0.500
US2	0.640	-0.165
US3	0.640	0.165
US4	0.640	0.500
US5	2.340	-0.990
US6	2.340	-0.330
US7	2.340	0.330
US8	2.340	0.990

Table I. Université Catholique de Louvain partial dam breach: gauge locations for recording the flow depth in the flume.